東北大学機関リポジトリ
TOUR
Tohoku University Repository

Physics at $t\bar{t}$ threshold in e+e- collisions

著者	隅野　行成
journal or publication title	Physical review. D
volume	50
number	7
page range	4341-4362
year	1994
URL	http://hdl.handle.net/10097/35281

doi: 10.1103/PhysRevD.50.4341

Physics at $t\bar{t}$ threshold in e^+e^- collisions

K. Fujii and T. Matsui
KEK, Tsukuba 305, Japan

Y. Sumino
Department of Physics, University of Tokyo, Tokyo 113, Japan
(Received 21 October 1993; revised manuscript received 20 May 1994)

We present the results from quantitative studies of physics at $t\bar{t}$ threshold, taking into account realistic experimental conditions expected at future linear e^+e^- colliders. A possible experimental strategy is illustrated for a sample case of m_t=150 GeV, where the importance of the measurements of both total and differential cross sections is emphasized for precision determinations of various parameters. The studies are based on a recently developed theoretical formalism which includes full $O(\alpha_s)$ corrections. An energy scan of 11 points with 1 fb^{-1} each allows us to measure the top mass and the strong coupling constant with statistical errors of Δm_t=0.2 GeV and $\Delta\alpha_s$=0.005, respectively. As for the top width, $\Delta\Gamma_t/\Gamma_t$=0.2 (stat) is expected, if both m_t and α_s are known. The measurement of the top momentum at some optimized energy point with 100 fb^{-1} reduces the error on α_s to $\Delta\alpha_s$=0.0015, provided that the $1S$ peak position is known from the threshold scan. The momentum measurement also improves the precision on the top width to $\Delta\Gamma_t/\Gamma_t$=0.04, if α_s is known from other sources. The forward-backward asymmetry in the threshold region provides another interesting method to measure α_s and Γ_t.

PACS number(s): 13.65.+i, 14.65.Ha

I. INTRODUCTION

The top quark is one of the most important physics targets at future linear e^+e^- colliders. As recent experimental limits on the top mass [1,2],

$$m_W < m_Z \lesssim m_t \lesssim 200 \text{ GeV}, \quad (1)$$

indicate, the top decays directly into bW, which essentialy saturates the branching fraction in the standard model and is dominant in most of its extensions. The dominance of the $t \to bW$ mode leads to a large top width which is about 0.8 GeV for $m_t = 150$ GeV and becomes as large as 2.2 GeV for $m_t = 200$ GeV. The most important new feature is probably this large top width that makes the top physics at future linear e^+e^- colliders unique. In the $t\bar{t}$ threshold region, the large top width acts as an infrared cutoff [3], which allows us a reliable estimate of cross sections based on *perturbative* QCD: the top decays before entering the nonperturbative regime and is insensitive to long-distance physics. Therefore, we can perform a clean test of QCD at the $t\bar{t}$ threshold. More importantly, since we can calculate the QCD contribution unambiguously, other smaller effects such as the Higgs boson exchange contribution may be extractable.

The basic physical parameters that enter the $t\bar{t}$ threshold physics are the top mass, the top width, and the strong coupling constant. In addition, we may include the top Yukawa coupling and the Higgs boson mass, when the Higgs boson exchange contribution is of observable size. The observation that the large top width acts as an infrared cutoff initiated serious feasibility studies on the measurements of these parameters. The first attempt was made theoretically on the total $t\bar{t}$ cross section [4], which was soon supplemented by experimental feasibility studies [5–8]. It was then pointed out that differential cross sections, the top momentum distribution [9,10], and the forward-backward asymmetry [11] in particular, provide information independent of what is extractable from the total cross section. In the course of these developments, it was recognized that the full next-to-leading order corrections to the total and differential cross sections are indispensable for providing reliable theoretical predictions that stand up to the expected experimental accuracy. Recently, the calculation of full next-to-leading order corrections has been completed [12–14], which include the contributions from final state interactions (gluon exchange between t and $\bar{b}$ or $\bar{t}$ and b and between b and $\bar{b}$) together with that from real gluon emissions. These new corrections modify the top quark differential cross sections nontrivially, affecting the parameter determinations significantly [13,14]: for example, it has been shown that at $\sqrt{s} = 2m_t$ the final state interactions reduce the top momentum by about 5%, which corresponds to an α_s shift of $\Delta\alpha_s \simeq 0.01$ if we are to extract α_s from the top momentum distribution. It turned out, however, that these corrections cancel out altogether in the total cross section at the next-to-leading order [12–14].

In this paper, we report quantitative studies on the determinations of physical parameters under realistic experimental conditions, according to the formalism given in Ref. [14], which includes the full next-to-leading order corrections [15]. We show the importance of the measurements of the top momentum distribution and the forward-backward asymmetry. It is demonstrated that the top momentum distribution is indeed measurable and is useful in the parameter determinations, when mea-

 ©1994 The American Physical Society

sured at the energy optimized by using the information from the total cross section measurement. We illustrate our strategy for such consistent measurements, taking a sample case of $m_t = 150$ GeV.

The paper is organized as follows. In Sec. II we briefly review the theoretical background on which the subsequent analyses are based. Section III discusses experimental determinations of various parameters through the measurements of the total and differential cross sections where complications such as smearing effects due to beam energy spread and beamstrahlung (which is the bremsstrahlung from beam particles due to the strong electromagnetic fields produced by opposing beam bunches) are taken into account. Finally, Sec. IV summarizes the results and concludes this paper. The formulas necessary for our numerical studies are collected in Appendix A, while Appendix B gives a brief description of our Monte Carlo simulation.

II. THEORETICAL BACKGROUND

The t and $\bar{t}$ quark pairs created in e^+e^- collision spread apart from each other and decay via electroweak interaction into bW^+ and $\bar{b}W^-$, respectively, at distance $\sim (m_t\Gamma_t)^{-1/2}$ before hadronization occurs [16,17]. The t and $\bar{t}$ quarks, being slow in the threshold region, are trapped by the attractive force mediated by multiple exchange of Coulombic gluons between them. Therefore, the $t\bar{t}$ threshold region is an ideal place to test the enhanced QCD interaction in the spacelike region without uncertainties from the low-energy regime of QCD.

The basic building block of the amplitude for $e^+e^- \to t\bar{t}$ near the threshold is the Green's function of nonrelativistic Schrödinger equation in the presence of the QCD potential:

$$\left[-\frac{\nabla^2}{m_t} + V(r) - \left(E + i\frac{\Gamma_\theta}{2}\right)\right] G(\mathbf{x}; E) = \delta^3(\mathbf{x}). \quad (2)$$

Here, $E = \sqrt{s} - 2m_t$ is the energy measured from the threshold. $r = |\mathbf{x}|$ denotes the relative distance between the t and $\bar{t}$ quarks, and the δ function on the right-hand side shows the creation of a $t\bar{t}$ pair at the same point. Γ_θ is the running toponium width [9], which is almost twice the top quark width Γ_t. (See Appendix A.)

Roughly, the QCD potential is given by the Coulombic potential with its running coupling constant evaluated at momentum scale $\mu \sim 1/r$:

$$V(r) \sim -C_F \frac{\alpha_s(1/r)}{r}. \quad (3)$$

The toponium resonances feel the attractive force corresponding to the coupling $\alpha_s(\mu)$ evaluated at the size of their wave functions, typically $\mu \sim \alpha_s m_t$ ~(Bohr radius)$^{-1}$. Since the top quark is heavy, its typical kinetic energy inside a $t\bar{t}$ bound state far exceeds those of quarks inside the lighter quarkonia. Therefore, the top quark can probe the deep region of the QCD potential.

The leading enhancement of the amplitude in the threshold region is attributed to the $t\bar{t}V(V = \gamma, Z)$ vector vertex $\Gamma^\mu_{t\bar{t}V}$, which is proportional to the above Green's function in momentum space [18,4]:

$$\Gamma^\mu_{t\bar{t}V} \propto \tilde{G}(\mathbf{p}; E), \quad (4)$$

$$\tilde{G}(\mathbf{p}; E) = \int d^3\mathbf{x}\, e^{-i\mathbf{p}\cdot\mathbf{x}} G(\mathbf{x}; E). \quad (5)$$

See Fig. 1. Using the resonance wave functions $\psi_n(\mathbf{x})$'s, which are the solutions to the homogeneous version of the Schrödinger equation [Eq. (2)] with energies E_n's, and their Fourier transforms $\phi_n(\mathbf{p})$'s, we may express the Green's function as

$$\tilde{G}(\mathbf{p}; E) \simeq -\sum_n \frac{\phi_n(\mathbf{p})\psi_n^*(\mathbf{x}=0)}{E - E_n + i\Gamma_n/2}. \quad (6)$$

A. Total cross section and momentum distribution

The total cross section for $e^+e^- \to t\bar{t}$ can be obtained via the optical theorem [3]

$$\sigma_{\rm tot} \propto {\rm Im}G(\mathbf{x}=0; E) \simeq -{\rm Im}\sum_n \frac{|\psi_n(\mathbf{0})|^2}{E - E_n + i\Gamma_n/2}. \quad (7)$$

We can see that the cross section exhibits a resonance spectrum as a function of the c.m. energy. The level gaps of the spectrum are of the order of $\Delta E \sim \alpha_s^2 m_t$, while the resonance widths are $\Gamma_n \simeq 2\Gamma_t$. For $m_t \gtrsim 150$ GeV, ΔE and Γ_n being of comparable size, various resonance states interfere with one another so that the resonance structure will be quite smeared. Thus, we are necessarily concerned with the overall shape of the total cross section in the threshold region.

On the other hand, one can measure the momentum distribution of the top quark in the threshold region by reconstructing the top quark momentum $\mathbf{p}$ from its daughter bW-jet momenta. In the leading order aproximation, the top quark momentum distribution is proportional to the square of the momentum-space Green's function:

$$\frac{d\sigma}{d|\mathbf{p}|} \propto |\tilde{G}(\mathbf{p}; E)|^2. \quad (8)$$

According to Eq. (6), we may measure the momentum-space wave functions of the toponium resonances using

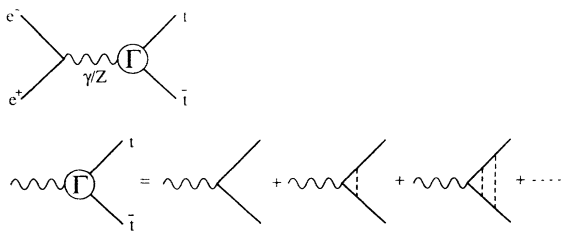

FIG. 1. Threshold correction to the $t\bar{t}$ pair production process.

the top quark momentum distribution. Thus, the momentum distribution provides information independent of that from the total cross section, so that it can be used to measure physical parameters near threshold.

B. Forward-backward asymmetry

It has been discussed recently that there will be measurable forward-backward (FB) asymmetry in the $t\bar{t}$ pair production near the threshold. At the leading order, the distribution of the top quark is known to be spherical. The FB asymmetry originates from the following two sources, which apper at the next-to-leading order.

1. S-P interference

The main contribution to the FB asymmetry comes from the interference of the vector and axial-vector vertices [11].

In the $e^+e^- \to t\bar{t}$ process, one can show from the spin-parity argument that the $t\bar{t}V$ $(V = \gamma, Z)$ vector vertex creates S- and D-wave resonance states, while the $t\bar{t}Z$ axial-vector vertex creates P-wave states. Since the P-wave amplitude is suppressed by a power of β near the threshold, its interference with the S-wave resonance states gives rise to an $O(\beta)$ correction to the leading S-wave contribution to the cross sections. Since this correction stems from the interference of the vector and the axial-vector couplings, it is porportional to $\beta\cos\theta$, thus producing FB asymmetry of $O(\beta) = O(\alpha_s)$.

In general, the S-wave and the P-wave resonance states have different energy spectra. If the c.m. energy is fixed at a resonance chosen from either one of the two spectra, there would be no contribution from the other. The widths of the resonances, however, grow rapidly as m_t increases, and they become so large that the S-wave and the P-wave resonance states start to interfere for $m_t \gtrsim 100$ GeV. This is the main origin of the FB asymmetry present even below the threshold, and provides information on the resonance level structure which is concealed in the total cross section due to the large smearing effect.

2. Final state interaction

There is also some contribution from the final state interactions (Fig. 2) to the FB asymmetry as a part of the next-to-leading order corrections. It turns out, however, that this contribution is small, at the level of 1–2% [14].

So, in essence, the FB asymmetry "measures" the degree of the overlap of the S-wave and the P-wave resonances.

In the following section, we analyze the total cross section, the momentum distribution, and the FB asymmetry on the basis of the above physical picture. We include the full next-to-leading order $[= O(\alpha_s)]$ corrections and the initial state radiation to the cross sections. The effects of beam energy spread and beamstrahlung are also examined. All the necessary formulas for the cross section evaluations are summarized in Appendix A.

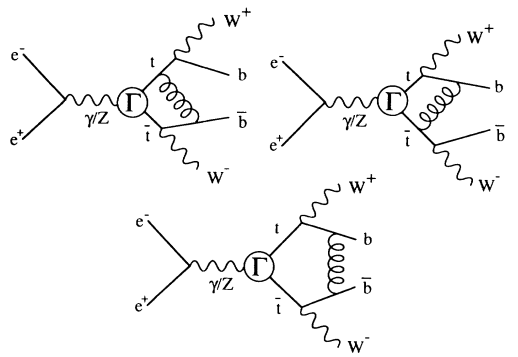

FIG. 2. Next-to-leading order corrections from final state interactions.

III. DETERMINATION OF VARIOUS PARAMETERS

In this section, we discuss how to determine various parameters involved in the $t\bar{t}$ threshold cross sections. We start with the measurement of the total cross section through threshold scan in Sec. III A. The threshold scan alone can provide fairly good measurements of various parameters, given a moderate integrated luminosity expected at the initial stage of linear e^+e^- collider experiments. The information gathered through the threshold scan is essential for the decision of the energy points to invest more luminosity (high luminosity top factory runs) and to perform differential cros section (top momentum distribution and forward-backward asymmetry) measurements. The energy points will be chosen so as to maximize the sensitivity to the parameters in question and to minimize the theoretical and experimental ambiguities. As we will see, the differential cross section measurements, the top momentum distribution in Sec. III B and the forward-backward asymmetry in Sec. III C, provide information which is independent of that from the total cross section and help us improve greatly the precision of the parameter determination.

Unless otherwise stated, we assume $m_t = 150$ GeV in what follows, which roughly corresponds to the current best estimate from precision electroweak measurements at the CERN e^+e^- collider LEP [2].

A. Threshold scan

1. Dependence of total cross section on various parameters

The total $t\bar{t}$ cross section in the threshold region involves the parameters

$$\sigma_{t\bar{t}}(\sqrt{s}, m_t, \Gamma_t, \alpha_s(m_Z), m_H, \beta_H), \tag{9}$$

where β_H is the top Yukawa coupling normalized by its

standard model value. We first examine how the threshold shape depends on these parameters, leaving out the beam effects.

As shown in Fig. 3(a), the first S-wave peak position shifts downward, while the peak itself is enhanced when α_s increases. This is because, when the potential becomes deeper, the binding energy and the wave function at the origin also become larger. Thus, the total cross section tends to behave similarly in two situations: (a) we increase α_s with m_t fixed, (b) we decrease m_t with α_s fixed.

On the other hand, the correlation between m_t and the top width Γ_t is small, as seen in Fig. 3(b). When the width becomes narrower, the peak height increases, while the tail part decreases. Notice that in Fig. 3(b), $|V_{tb}|^2$ is defined by

$$|V_{tb}|^2 = \Gamma_t/\Gamma_t(SM : |V_{tb}|^2 = 1), \tag{10}$$

and can be greater than unity when there is (nonstandard model) additional decay modes such as $t \to bH^+$ or $t \to \tilde{t}\tilde{X}^0$ or both.

The most interesting is the Higgs boson effect. Since this effect can be implemented to the first approximation by adding to the QCD potential an attractive Yukawa potential

$$V_H(r) = -\frac{\sqrt{2}G_F}{4\pi}(\beta_H m_t)^2 \frac{e^{-m_H r}}{r}, \tag{11}$$

the Higgs-boson-exchange contribution is expected to be large for smaller m_H and larger β_H. Notice that the range of this potential is controlled by the Higgs boson mass (m_H) and is short compared to the QCD potential. Therefore, the Yukawa potential does not change the resonance position very much, but makes the wave function at the origin significantly larger, thereby making the cross section larger everywhere in the threshold region. The potential approximation is, however, known to be inappropriate for $m_H > 50$ GeV: the potential approximation significantly overestimates the Higgs boson effects for large m_H. We, therefore, evaluate the Higgs boson effects, according to the prescription recently proposed in Ref. [19]. Namely, we include the Yukawa potential [Eq. (11)] in the calculation of the Green's function, and then multiply the cross section [$\propto \mathrm{Im}G(0;E)$] as

$$\mathrm{Im}G(0;E) \to |F_{\mathrm{Higgs}}(m_H^2/m_t^2)|^2 \mathrm{Im}G(0;E), \tag{12}$$

where the hard Higgs boson correction factor is given by

$$F_{\mathrm{Higgs}}(m_H^2/m_t^2) = 1 + \frac{\alpha\beta_H^2}{4\pi\sin^2\theta_W}\left(\frac{m_t^2}{m_W^2}\right) \times \left(f_{\mathrm{th}}(m_H^2/m_t^2) - \pi\frac{m_t}{m_H}\right). \tag{13}$$

The function f_{th} is defined by

$$f_{\mathrm{th}}(r) = -\frac{1}{12}\left[-12 + 4r + (-12 + 9r - 2r^2)\ln r + \frac{2}{r}(-6 + 5r - 2r^2)l_4(r)\right] \tag{14}$$

with

$$l_4(r) = \begin{cases} \sqrt{r(4-r)}\arccos(\sqrt{r}/2) & \text{if } r \le 4, \\ -\sqrt{r(r-4)}\,\frac{1}{2}\ln\frac{1+\sqrt{1-4/r}}{1-\sqrt{1-4/r}} & \text{otherwise.} \end{cases} \tag{15}$$

Figures 3(c) and 3(d) demonstrate the dependences on m_H and β_H, respectively. We can see that the above qualitative observations, which were made based on the potential approximation, still hold.

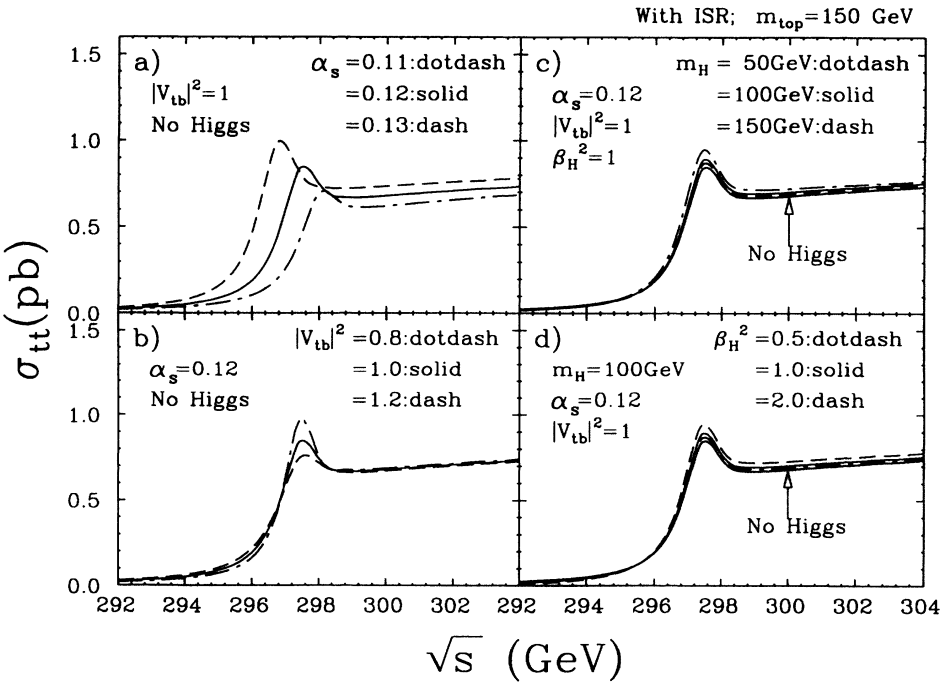

FIG. 3. Dependence of the threshold shape on (a) $\alpha_s(m_Z)$, (b) $|V_{tb}|^2$, (c) m_H, and (d) β_H (the normalized Yukawa coupling), in the case of $m_t = 150$ GeV. Initial state radiation is incorporated in the figures.

2. Dependence on intermediate-distance potential

It is of importance to confirm that the threshold shape is essentially determined by the short-distance part of the potential, which is derived from perturbative QCD, and is insensitive to the shape of the potential in intemediate- and long-distance regions. We will examine here the dependence on the change in the intermediate-distance potential.

It is well known that the data from charmonium and bottomonium spectroscopy are best reproduced when we take a logarithmic function of r as the intermediate-distance potential [20]. The intermediate-distance part of our potential is determined by fitting to the charmonium and bottomonium data, which smoothly continues to the QCD-motivated short-distance potential at $r = r_0$, where r_0 is one of the adjustable parameters to specify the potential shape [9]. Since r_0 affects most significantly the intermediate-distance potential, we change it by ± 5 standard deviations away from its best fit value [21], while keeping the short-distance potential fixed, and see how much the threshold shape changes. As shown in Fig. 4(a), this modification of the intermediate-distance potential does not alter the threshold shape at all. When the top quark width is artificially reduced to 1/10, the difference is visible for higher resonance states [see Fig. 4(b)]. This clearly demonstrates that the large top quark width actually acts as an infrared cutoff and the theoretical prediction of the threshold shape is indeed insensitive to the intermediate-distance potential.

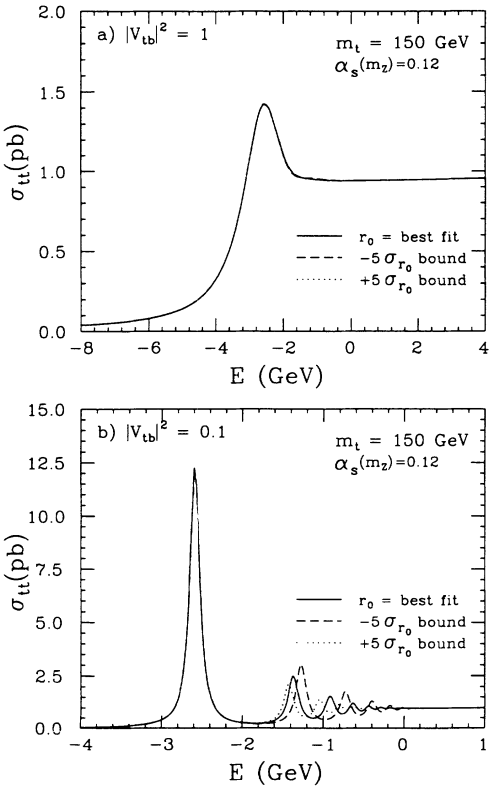

FIG. 4. Dependence of the threshold shape on the intermediate-distance potential for (a) $|V_{tb}|^2 = 1$ and (b) $|V_{tb}|^2 = 0.1$. The figures are before the inclusion of initial state radiation and beam effects.

3. Beam effects

What we will actually observe at a future linear e^+e^- collider is the convolution of the threshold shape presented above with the beam energy spectrum in Fig. 5 (see Appendix A). The tail towards the low-energy region is the result of beamstrahlung. On the other hand, the sharp peak at the nominal center-of-mass energy $\sqrt{s_0}$ corresponds to collisions with no beamstrahlung. The width of this sharp peak is determined by beam energy spread. Both the beam energy spread and the beamstrahlung affect the observable threshold shape. It is, therefore, very important to examine the effects of the beam energy spread and the beamstrahlung for designing the collider and the experiment therewith. Since the effect of the beamstrahlung is expected to be similar to that of the initial state radiation, we will examine how the cross section changes in three steps: (i) no initial state radiation (ISR) and no beam effects, (ii) with the ISR but without the beam effects, and (iii) with both of the ISR and the beam effects.

We can see in Fig. 6 that the ISR reduces the observable cross section significantly, though the $1S$ peak is still visible. The beam effects, the beam energy spread in particular, smear out the $1S$ peak. The main effect of the beamstrahlung is, in this case, a loss of usable luminosity.

Since the beam energy spread appers to be the major problem with our planned precision measurements, we should also be aware of the effects of the structure inside the δ-function part which corresponds to the no beamstrahlung case. In order to see the effects more clearly, we switch off the beamstrahlung here and examine how the threshold shape changes with the beam energy spread for two kinds of spectra, flat-top and double-peak, which is more realistic. Figure 7(a) is the enlargement of the δ-function part for these two spectra with various beam energy widths, and Fig. 7(b) is the corresponding thresh-

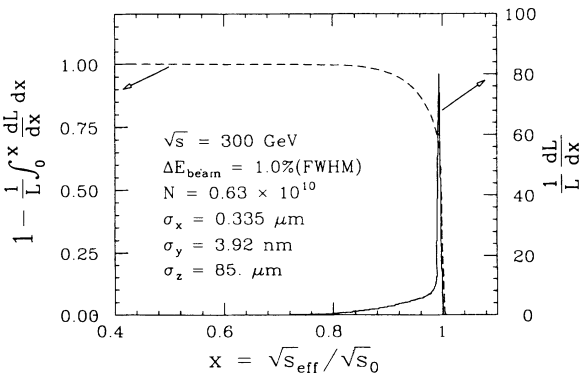

FIG. 5. Differential luminosity as a function of the center-of-mass energy after the inclusion of beam energy spread and beamstrahlung.

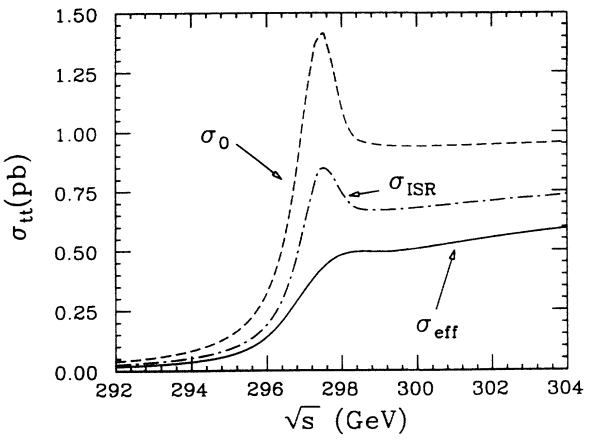

FIG. 6. Effects of the initial state radiation and the beam energy spread and beamstrahlung on the threshold shape for $m_t = 150$ GeV and $\alpha_s(m_Z) = 0.12$: with no ISR and no beam effects (dash), with ISR but without beam effects (dotdash), and with both ISR and beam effects (solid).

old shape. We can see that, when the beam energy spread is greater than 0.4%, the structure inside the δ-function part affects the threshold shape.

The beam effects can be summarized as follows. (i) The beamstrahlung reduces the usable luminosity in the threshold region. In other words, the usuable part is essentially restricted to the δ-function part. Therefore, we need to know the height of the δ-function part accurately for precision measurements. (ii) The beam energy spread is the major source of the peak smearing. When the energy spread is less than 0.4%, however, the threshold shape is practically independent of the structure inside the δ-function part. If we cannot achieve such a narrow band beam, it is important to measure the spectrum inside the δ-function part with a high-energy resolution [22].

4. *Event selection*

The signature of $t\bar{t}$ pair production is two b quarks and two W bosons in the final state. The two W bosons decay into either $q\bar{q}'$ or $l\bar{\nu}$. Therefore the final state configurations are (i) two b jets and four jets from W's (45%), (ii) two b jets, two jets, and one charged lepton (44%), and (iii) two b jets and two charged leptons (11%). Case (i) is useful for the total cross section and the momentum distribution measurements, while case (ii) is the only channel to measure the forward-backward asymmetry in practice. The basic cuts used in these analyses can be classified into the following three groups: (a) event shape cuts such as those on the number of charged particles, the number of jets, and thrust, (b) mass cuts to select W's and t's by jet-invariant-mass method, and (c) requirements of leptons in cases (ii) or (iii). If available, b tagging is a powerful tool to reduce the combinatorial background in the parton reconstruction by jet-invariant-mass method.

In order to measure the threshold shape reliably, we need to select $t\bar{t}$ events with a good signal-to-background ratio. For our choice of the beam-related parameters, the effective cross section at the threshold is about 0.5 pb for $m_t = 150$ GeV, while that of the largest background (W^+W^- productions) is about 14 pb. We need some 10^{-3} suppression.

To see how this can be achived, we took case (i) as an example and carried out Monte Carlo simulations (see Appendix B). Figure 8(a) shows a tyical 6-jet event expected for case (i). Its calorimetric lego plot is in Fig. 8(b), where we can clearly see six jets.

Our event selection proceeds as follows. We first require 20 or more charged tracks and impose cuts on the visible energy (the energy sum of all the detected particles including neutral ones) and the total transverse momentum: $E_{\rm vis} \geq 200$ GeV and $p_T \leq 50$ GeV. The remaining events must contain six or more hadronic jets after jet clustering with $y_{\rm cut} = 5 \times 10^{-3}$, where $y_{\rm cut}$ is the cut on jet-invariant masses normalized by the visible energy. When there are more than six jets, we increase the $y_{\rm cut}$ value so as to make the event yield exactly six jets. Two pairs of jets out of these six jets must have 2-jet invariant masses consistent with m_W. These two W

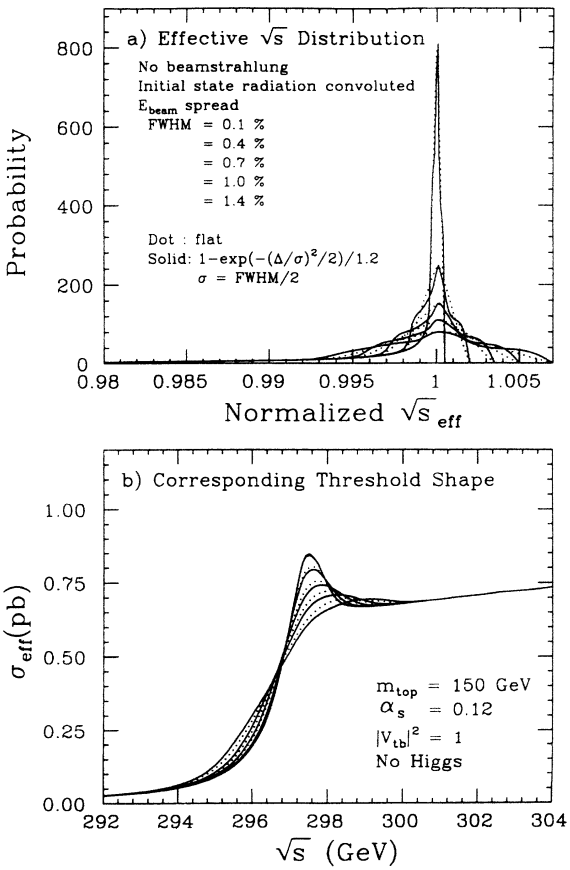

FIG. 7. (a) Reduced center-of-mass energy distributions including the effects of initial state radiation and natural beam energy spread but leaving out the effect of beamstrahlung. Distributions for two kinds of spectra, flat-top and double-peaked, which is more realistic, are shown for various beam energy spreads. (b) Corresponding theshold shapes.

candidates are then required to make invariant masses consistent with m_t, when combined with one of the remaining two jets. (The locations of these mass cuts will be shown in Figs. 10 and 11 below.) Finally we impose a cut on the event thrust: thrust$\leq$ 0.75.

Histogrammed in Figs. 9(a) and 9(b) are the visible energy and the total transverse momentum for the initial sample of $t\bar{t}$ events (20k events), respectively, where the final $t\bar{t}$ sample distributions after all the cuts are also shown as hatched histograms. Figure 10 is the scatter plot of the 2-jet invariant masses corresponding to two W candidates for the final $t\bar{t}$ sample where their projections are also shown. The cut on the invariant masses is depicted as a square in the figure. Figure 11 is a similar plot for the 3-jet invariant masses corresponding to the bW candidates at the threshold. The smooth curve indicates the location of the m_t cut. Finally, Fig. 12 shows the thrust distribution for the $t\bar{t}$ sample (open histogram) just before the final thrust cut. The hatched histogram in the same figure is the remnant W^+W^- background which can be effectively suppressed with the thrust cut indicated by an arrow. After this final cut, the detection efficiency is 29% while the signal-to-background ratio is greater than 10. This detction efficiency translates to about 63% when the $W \to q\bar{q}$ branching ratio of 67% is taken into account. Although we can obtain similar efficiencies and signal-to-background ratios for cases (ii) and (iii), we conservatively assume this efficiency in the following section.

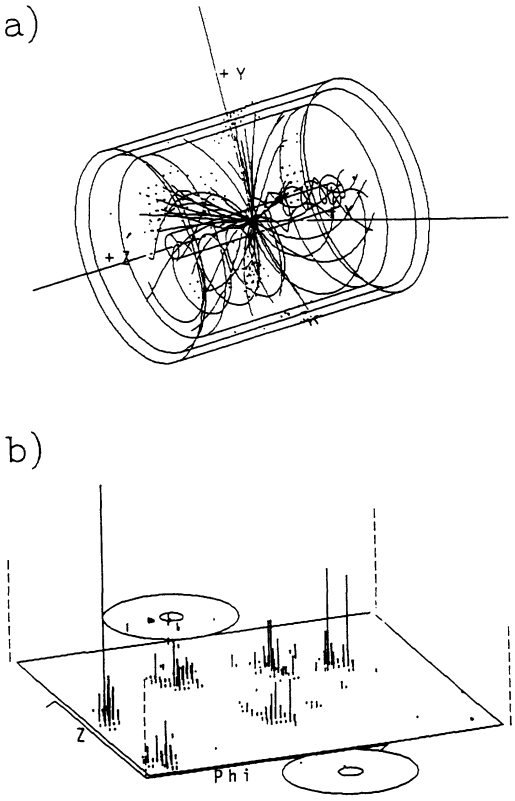

FIG. 8. (a) Typical 6-jet event from $e^+e^- \to t\bar{t} \to bW^+\bar{b}W^-$ where both W^+ and W^- decay into $q\bar{q}$. (b) The same event in the calormeter.

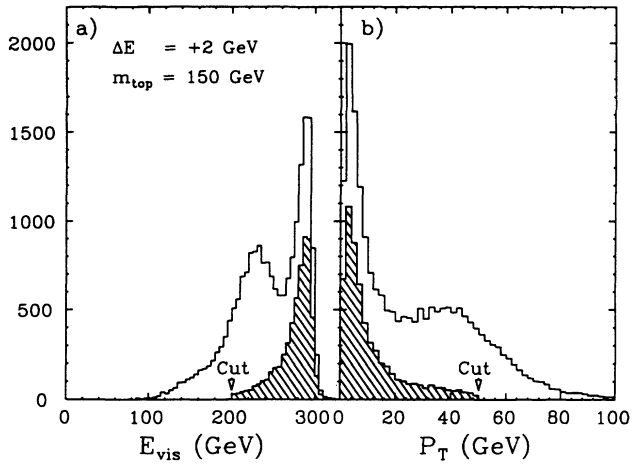

FIG. 9. (a) $E_{\rm vis}$ and (b) P_t distributions for initial (open histograms) and final (hatched histograms) samples.

5. *Expected experimental sensitivity*

Using the $t\bar{t}$ sample so obtained, we can determine the physical parameters that enter the threshold formula. Experimental feasibility of such a measurement has been studied by several authors [5–8]. We show below the results of our study using the new formalism summarized in Appendix A.

Figure 13(a) is an example of the energy scan to determine m_t and $\alpha_s(m_Z)$. Each data point corresponds to 1

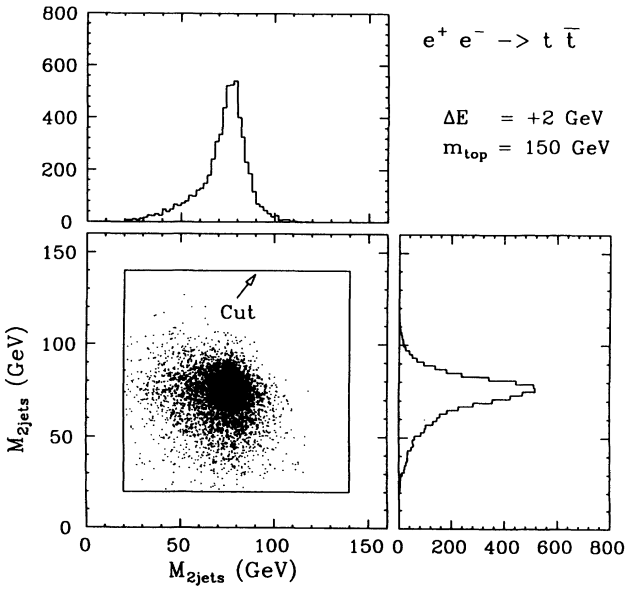

FIG. 10. A scatter plot of the invariant masses of the 2-jet systems reconstructed as W boson candidates together with their projection to each axis.

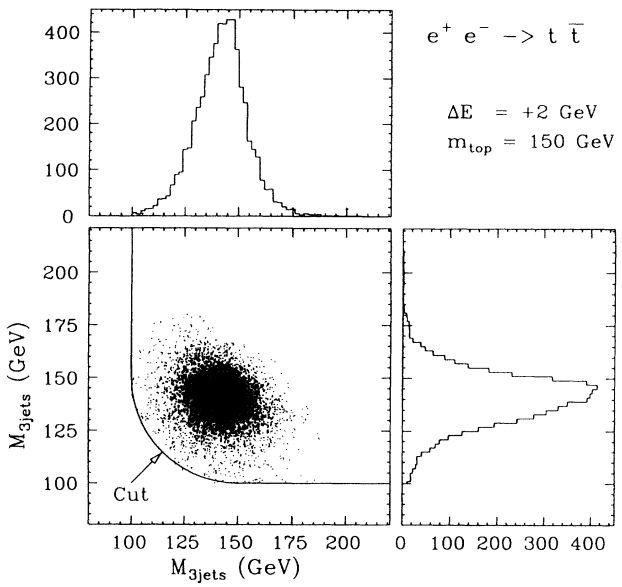

FIG. 11. A similar plot for the invariant masses of the 3-jet systems reconstructed as bW candidates.

fb^{-1} and was generated with $|V_{tb}|^2 = 1$, $\alpha_s(m_Z) = 0.12$, and $m_H = \infty$(no Higgs boson). By fitting these data points to the threshold formula convoluted with the natural beam energy spread and the beamstrahlung spectra, we obtain a contour plot shown in Fig. 13(b). The strong correlation between m_t and $\alpha_s(m_Z)$ stems from the fact that the resonance mass decreases as $\alpha_s(m_Z)$ increases. If $\alpha_s(m_Z)$ is known, we have $\Delta m_t \simeq 0.1$ GeV and even if $\alpha_s(m_Z)$ is totally unconstrained, we can expect $\Delta m_t \simeq 0.2$ GeV. On the other hand, the expected statistical error on the strong coupling constant is $\Delta\alpha_s(m_Z) = 0.005$, when there is no other measurement on m_t.

Figure 14(a) is a similar plot for the determination of $|V_{tb}|^2$. Again we assume 1 fb^{-1} per point. The corresponding contour plot [Fig. 14(b)] shows no correlation between m_t and $|V_{tb}|^2$ and indicates $\Delta|V_{tb}|^2 \simeq 0.15 \sim 0.20$.

Figures 15(a) and 15(b) are examples of the m_H and β_H measurements where the energy points are chosen in the same way as with Figs. 13(a) and 14(a). The m_H-β_H^2 contours are given in Fig. 15(c) where the solid and dashed lines correspond to 1 fb^{-1} and 2 fb^{-1} per point, respectively. We note that, when we use the lepton-plus-4-jet mode together with the 6-jet mode, the detection efficiency almost doubles and the contours for 1 fb^{-1} per point roughly become the dashed lines. For the standard model Higgs boson of $m_H = 100$ GeV, the expected error on β_H is $\Delta\beta_H = 0.43$ and 0.29 for 1 fb^{-1} and 2 fb^{-1} per point, respectively.

It should be noted that the energy points used here are by no means optimized. Prior to the actual energy scan, we will have a fairly good estimate of m_t from the measurement of the 3-jet invariant mass [6,7]. Based on this knowledge, we should be able to improve the precision of the measurements by optimizing the energy points to maximize the sensitivities to the model parameters discussed above.

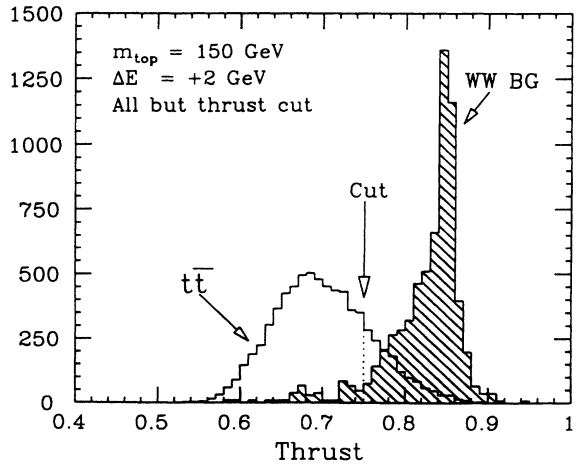

FIG. 12. Thrust distributions for the $t\bar{t}$ signal and the W^+W^- background with all but the thrust cut indicated by an arrow.

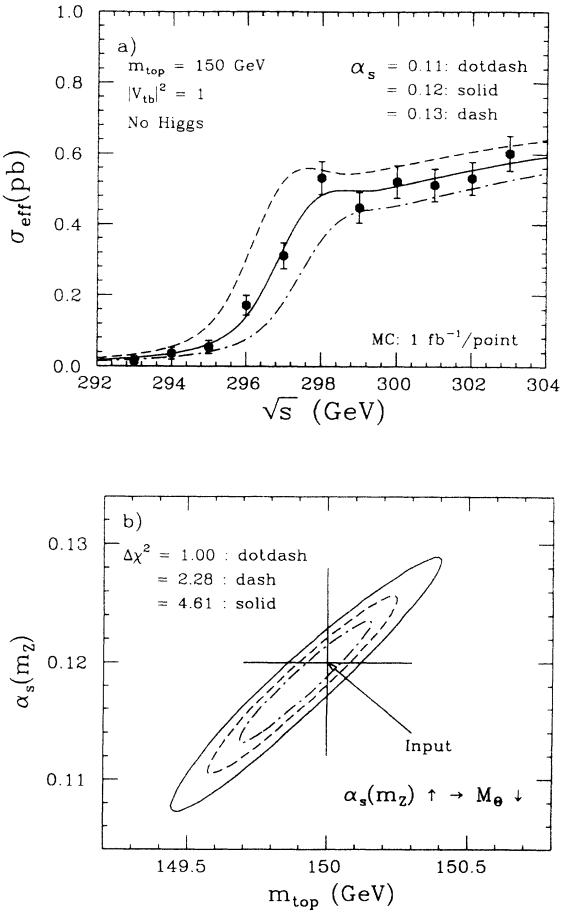

FIG. 13. (a) An example of energy scan to determine m_t and $\alpha_s(m_Z)$ where each point corresponds to 1 fb^{-1}. (b) The contour resulting from the fit to the data points.

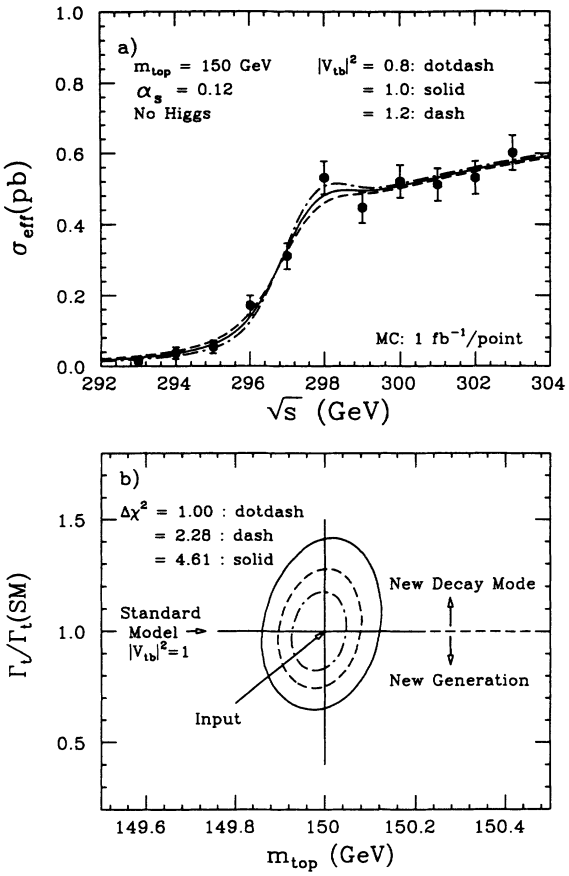

FIG. 14. (a) An example of energy scan to determine m_t and $|V_{tb}|^2$ where each point corresponds to 1 fb^{-1}. (b) The contours resulting from the fit to the data points.

B. Measurement of momentum distribution

By virtue of the large top quark width, we can measure the top quark momentum by reconstructing the 3-jet decay of a top quark, even below the $t\bar{t}$ threshold. This is in contrast to the charmonium and bottomonium cases, where the annihilation modes dominate. As Eqs. (6) and (A3)–(A5) indicate, the top momentum distribution provides information on the momentum-space wave functions of the toponium resonances. On the other hand, the total cross-section measurement only probes the wave functions at the origin [see Eq. (7)]. The momentum measurement thus allows us to extract additional information for parameter determinatons. It should be emphasized that the toponium is the first quarkonium that enables us to measure the momentum-space wave function.

Before discussing the sensitivity of the top momentum measurement to various parameters, we need to fix the energy point at which the momentum measurement is to be performed. The choice of the energy point should be made from the viewpoint of insensitivity to theoretical ambiguities and beam effects and sensitivity to physical parameters to be determined. Up to this point, we have been using the energy measured from the threshold ($E = \sqrt{s} - 2m_t$) which depends on m_t. There is, however, a strong correlation between α_s and m_t in the total cross section measurement. Moreover, the definition of m_t has a theoretical ambiguity of ~ 300 MeV due to the ambiguity in the constant term of the QCD potential: the charmonium and bottomonium data only constrain the slope of the potential [23]. There remains, therefore, some ambiguity in the definition of the threshold position. This difficulty can be avoided, if we measure the energy from the $1S$ peak position which can, in principle, be fixed by the threshold scan. For simplicity, we assume, in what follows, that the $1S$-peak position ($\sqrt{s_{1S}}$) is known and use $\Delta E = \sqrt{s} - \sqrt{s_{1S}}$ to specify the energy point.

1. *Dependence of momentum distribution on various parameters*

Since the Higgs boson exchange contribution is of short range and only affects the overall normalization of the

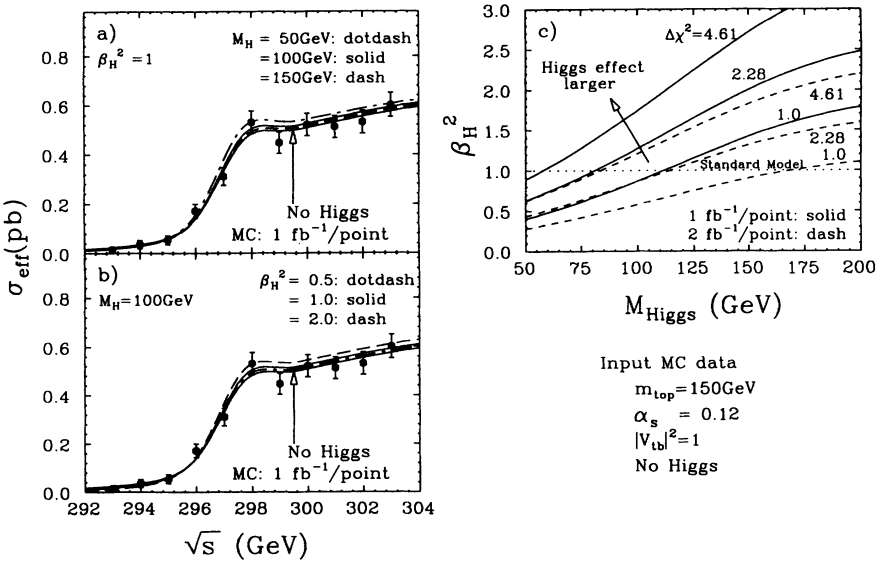

FIG. 15. (a) An example of energy scan to determine M_H and β_H^2 where the effective cross-section curves are superimposed for several M_H values. (b) The same plot with the effective cross-section curves for several β_H^2 values. (c) The contour resulting from the fit to the data points. The solid and dashed lines correspond to 1 fb^{-1} and 2 fb^{-1} per point, respectively.

cross section, the shape of the momentum distribution is insensitive to the Higgs boson effects. The relevant parameters are thus m_t, Γ_t, and $\alpha_s(m_Z)$. We will first examine the dependece of the top momentum distribution on these parameters before the inclusion of the beam effects.

Figure 16 shows how the momentum distribution changes with α_s at the $t\bar{t}$ threshold ($E = 0$). The peak momentum $|\mathbf{p}|_{\rm peak}$ increases with α_s. This behavior is expected from the virial theorem which predicts that the average top momentum is roughly given by $\alpha_s m_t$. When we plot the momentum peak position as a function of ΔE, however, this naive expectation is no longer valid, since the $1S$-peak position (E_{1S}) varies rapidly with α_s: $E_{1S} \sim -\alpha_s^2 m_t$. This rapid change of $\sqrt{s_{1S}}$ overcompensates the $|\mathbf{p}|_{\rm peak}$ shift at a fixed ΔE and the correlation between $|\mathbf{p}|_{\rm peak}$ and α_s is reversed [23]. Figure 17(a) shows the dependence of $|\mathbf{p}|_{\rm peak}$ on ΔE for various $\alpha_s(m_Z)$ values.

The dependence on the normalized top width ($|V_{tb}|^2$) is shown in Fig. 17(b), where the peak shifts toward the higher momentum side when the top width gets larger. This is because, when the width grows, the top decays at shorter distance where the $t\bar{t}$ potential is deeper.

Figure 17(c) again plots $|\mathbf{p}|_{\rm peak}$ as a function of ΔE but, this time, for different values of m_t. Give the precision expected for m_t from the threshold scan, we can practically ignore the m_t dependence. Notice that this is so only when we fix the center of mass energy at a constant ΔE. The momentum measurement thus provides us with another handle to determine $\alpha_s(m_Z)$ and Γ_t with virtually no ambiguity caused by m_t uncertainty.

2. Beam effects

Since the momentum distribution depends heavily on the energy, the beam effects must be properly taken into account. In Fig. 18(a) we compare the top momentum distributions in the three cases considered for the total cross section: (i) no ISR and no beam effects, (ii) with the ISR but beam effects, and (iii) both the ISR and the beam effects. Despite the significant change in the low momentum region, the peak momentum position is rather stable against the ISR and the beam effects. To see this more quantitatively, we plot $|\mathbf{p}|_{\rm peak}$ in Fig. 18(b) as a function of ΔE for the three cases. The figure demonstrates that $|\mathbf{p}|_{\rm peak}$ is indeed quite insensitive to the beam effects, if we sit at sufficiently high energy: $\Delta E \gtrsim 1.5$ GeV in our case.

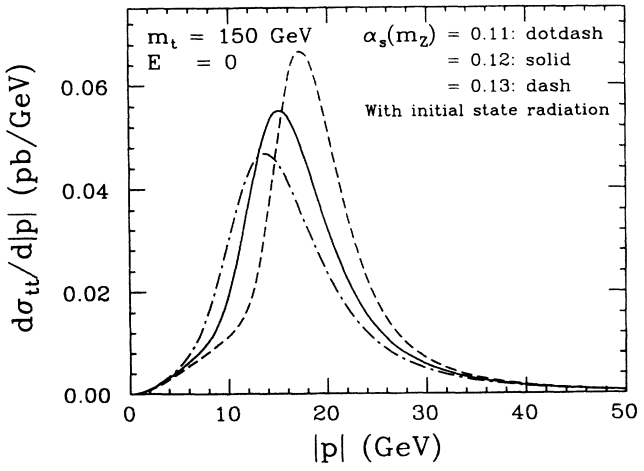

FIG. 16. Dependence of the top momentum distribution at the $t\bar{t}$ threshold on $\alpha_s(m_Z)$ in the case of $m_t = 150$ GeV.

3. Dependence on intermediate-distance potential

We have shown that the intermediate-distance potential has practically no effect on the total cross section. We cannot, however, conclude that this is also true for the momentum distribution. Figure 19 compares the momentum distributions, after the inclusion of the beam effects, at three different energy points ($\Delta E = 0, +2, +4$ GeV) with those for which r_0 is displaced by ± 5 stan-

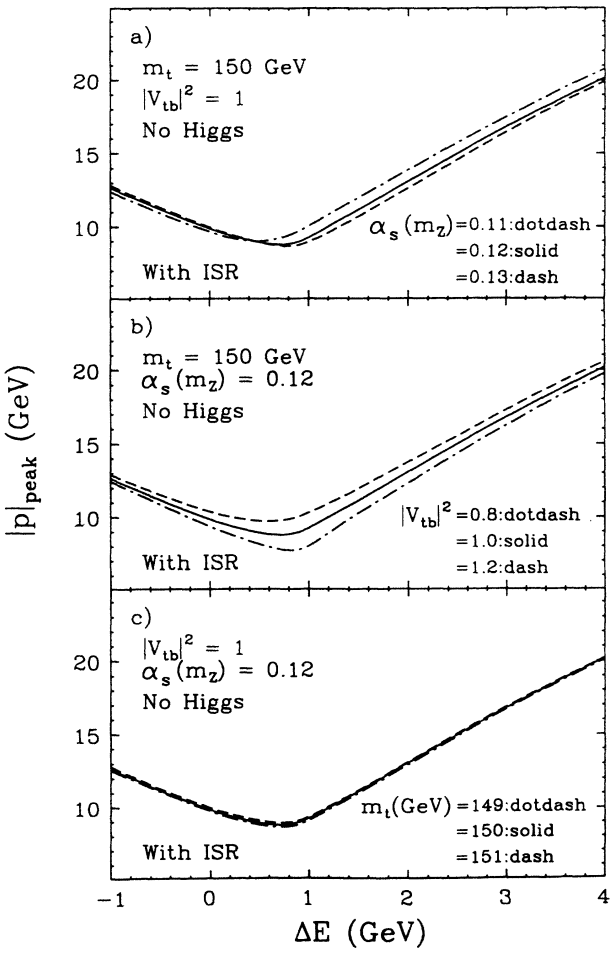

FIG. 17. Momentum peak position ($|\mathbf{p}|_{\rm peak}$) as a function of the energy measured from the $1s$ peak (ΔE) plotted to show the dependence on (a) $\alpha_s(m_Z)$, (b) $|V_{tb}|^2$, and (c) m_t. These include the initial state radiation but not the beam effects.

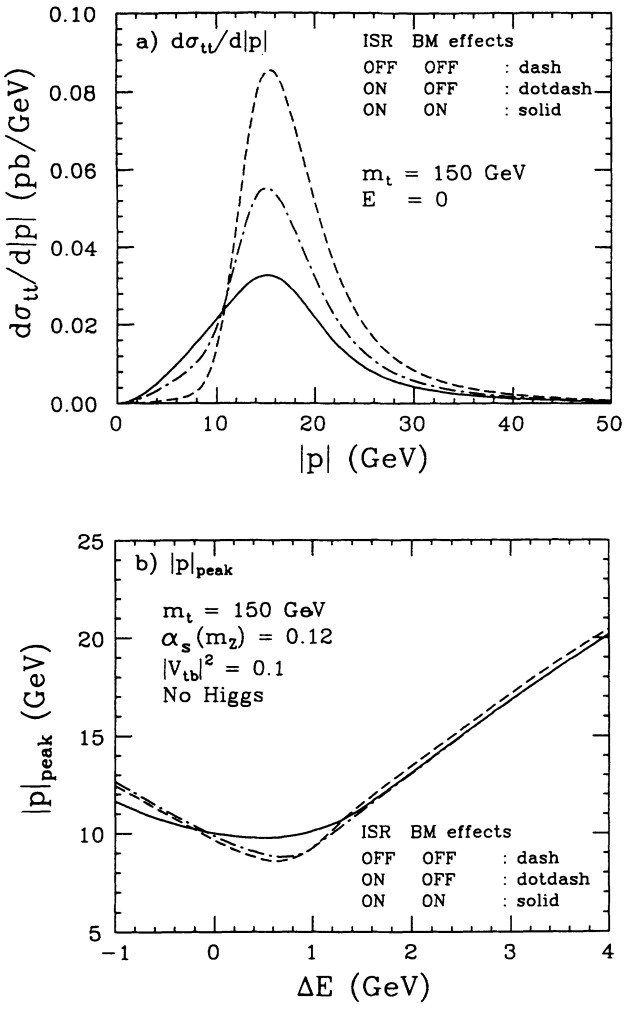

FIG. 18. (a) Effects of the initial state radiation and the beam energy spread and beamstrahlung on the momentum distribution. (b) Their effects on $|\mathbf{p}|_{\text{peak}}$.

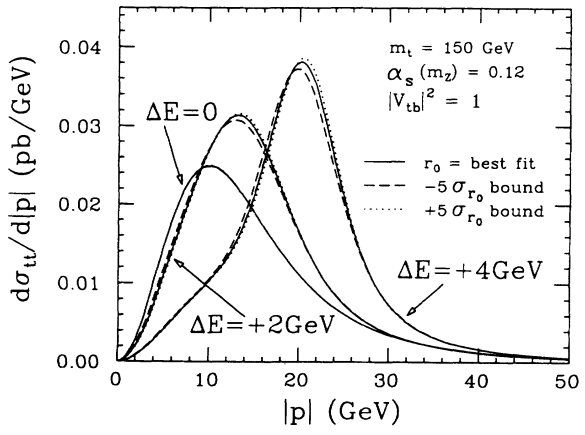

FIG. 19. Dependence of the momentum distribution on the intermediate-distance potential, after the inclusion of the initial state radiation and beam effects.

dard deviations from the best fit value. Since the short-distance potential essentially determines the wave functions of low-lying resonances, the modification of the intermediate-distance potential has virtually no effects on the momentum distribution at the $1S$ peak ($\Delta E = 0$). At $\Delta E = +2$ and $+4$ GeV, however, the modification produces a slight difference in the shape of the momentum distribution. The shifts in r_0 of ± 1 standard deviation induce shifts in the momentum peak position of $\pm 40(60)$ MeV at $\Delta E = +2(4)$ GeV. Although these systematic shifts are rather small, we had better choose the energy point near the $1S$ peak, in order to reduce the ambiguity introduced by this effect of the intermediate-distance potential. At all events, only the short-distance potential can be determined from perturbative QCD.

4. Sensitivity to various parameters

We have shown in Figs. 17(a)–17(c) how $|\mathbf{p}|_{\text{peak}}$ depends on $\alpha_s(m_Z)$, $|V_{tb}|^2$, and m_t. The corresponding figures after the inclusion of the beam effects are given in Figs. 20(a)–20(c). As mentioned above, the effects of the beam energy spread and beamstrahlung are significant

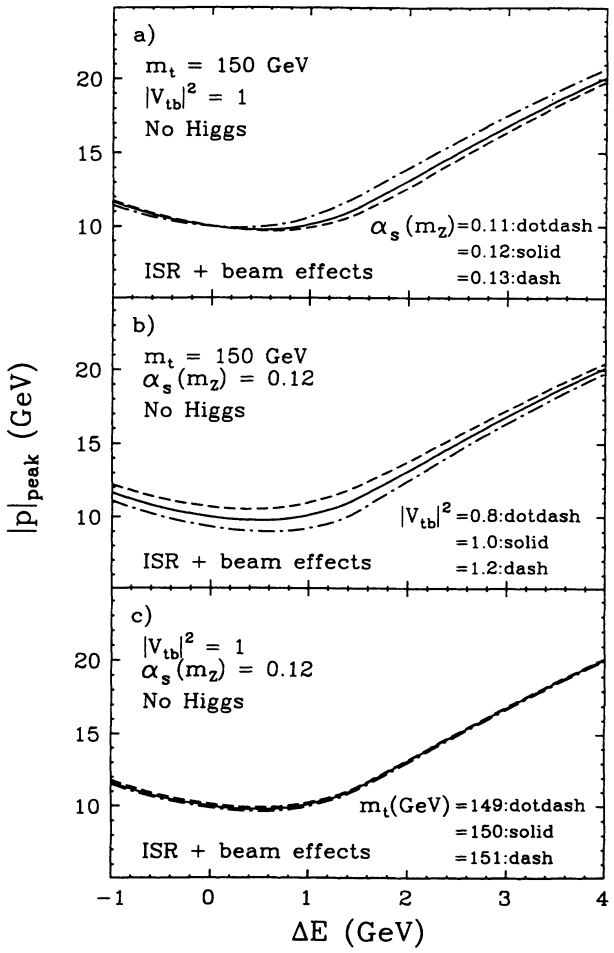

FIG. 20. The same as Figs. 17(a)–17(c), but with the beam effects.

only in the energy region $\Delta E < 1.5$ GeV. On the other hand, the sensitivity to $\alpha_s(m_Z)$ attains its maximum at around $\Delta E = 2$ GeV and stays essentially the same if we further increase the energy: notice that for $m_t = 150$ GeV the effective total cross section with beam effects depends only weakly on ΔE and so does the statistical error in the momentum measurement. The optimal energy, which maximizes the sensitivity to $\alpha_s(m_Z)$, while keeping small the beam effects and the dependence on the intermediate-distance potential, is thus $\Delta E = 2$ GeV for $m_t = 150$ GeV. As for the width measurement, a slightly lower energy is preferred. Since the sensitivity to the width is not much worse at $\Delta E = 2$ GeV, we fix the energy for the momentum measurement at $\Delta E = 2$ GeV in the following.

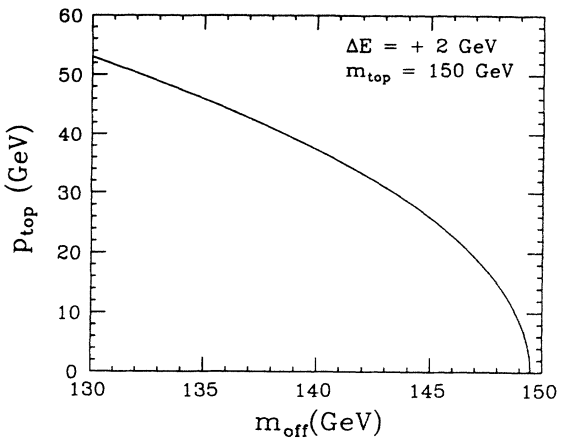

FIG. 21. Top momentum as a function of the invariant mass of the offshell top quark at $\Delta E = 2$ GeV.

5. *Event selection*

In order to measure the top momentum, we need to select top quarks which are well-reconstructed as 3-jet systems from $t \to bW$ decays. This requires final states with at least one t or $\bar{t}$ quarks decaying into three jets: configurations (i) and (ii) of Sec. III A 4. The 6-jet mode [case (i)] is advantageous from the statistical point of view, since both t and $\bar{t}$ quarks in a single event can be used for the momentum measurement. This mode, however, tends to suffer from combinatorial background: even if we have a perfect b-tagging capability, some ambiguity would still remain in assigning other four jets to two W's. The lepton-plus-4-jet mode [case (ii)] is cleaner in this respect. Therefore, we first consider case (ii).

The event selection starts with the requirement of an energetic ($E > 20$ GeV) electron or muon and at least four hadronic jets at $y_{\rm cut} = 5 \times 10^{-3}$ well within the detector acceptance. When there are more than four jets in the final state, the $y_{\rm cut}$ is understood to be increased to yield just four jets. Two out of the four jets must be tagged as heavy flavored by the impact parameter method: tagging efficiencies of 0.78 and 0.38 are assumed for b and c jets, respectively [24]. The two tagged jets are b-jet candidates. The invariant mass of the remaining two jets must be consistent with the W mass: $|M_{2\ \rm jets} - m_W| \leq 20$ GeV. Since t and $\bar{t}$ quarks are slow in the threshold region, the b quark and the W boson from a single top decay are expected to be nearly back-to-back. We note this and impose a cut on the b-W angle to select the b-jet candidate to be attched to the W candidate: $\cos\theta_{bW} \leq -0.75$. To minimize the misassignment of a wrong b jet to the W candidate, we demand that the two b-jet candidates are well separated: $\cos\theta_{bb} \leq 0.70$.

The above selection criteria provide a very clean sample of top quarks. This is, however, not enough for the momentum measurement. We have to make sure that the momentum of a reconstructed top quark is well measured. The rejection of events with energetic missing neutrinos is thus necessary. This forces us to apply a cut on the 3-jet invariant mass of the reconstructed top quark. This cut should, however, be applied with care, since the invariant mass cut in principle biases the momentum measurement. Figure 21 plots the top-quark momentum as a function of the mass of the off-shell one: notice that the dominant configuration below threshold is that one of t and $\bar{t}$ is on-shell and the other off-shell. The invariant mass cut should be loose enough not to affect the measurement in the momentum range of interest: $p \lesssim 30$ GeV. The following mass cut satisfies this condition: $|M_{3\ \rm jets} - m_t| \lesssim 15$ GeV.

Figure 22 plots the residuals of the reconstructed top momenta against the generated top momenta for $20k$ (corresponding to ~ 40 fb^{-1}) Monte Carlo $t\bar{t}$ events generated by the Monte Carlo programs described in Appendix B. The corresponding detection efficiency is 4%, including the branching fraction to the lepton-plus-4-jet mode. In the momentum reconstruction, we primarily used the central tracking device for charged tracks. The calorimeter information was used only for neutral clusters which have no matched charged tracks. The average of the residuals is shown in Fig. 23(a) as a function of the generated top momentum. In the low momentum region, the reconstructed top momentum is systematically higher than the generated one, since we are dealing with the absolute value of the top momentum. On the other

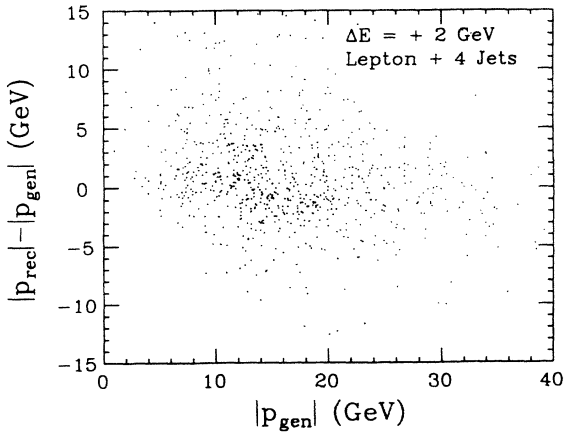

FIG. 22. Difference of the reconstructed and the generated top momenta plotted against the generated momentum for the lepton-plus-4-jet mode.

hand, missing neutrinos are epxected to reduce the reconstructed momentum in the higher momentum region. These systematic shifts are less than 1 GeV in the peak region of the momentum distribution. The momentum resolution is plotted in Fig. 23(b) again as a function of the reconstructed top momentum. The resolution is 3–4 GeV in the relevant momentum range, which is much less than the width of the momentum distribution.

Figure 24(a) compares the distribution of the reconstructed top momenta (solid circles) after all the cuts with that of the generated ones (histogram) before any cuts, where the generated distribution has been scaled to match the total number of detected events. Although the reconstructed top momenta are plotted with no corrections for resolution and cut effects, the agreement is fairly good. Plotted with solid squares are the combinatorial background due to wrong jet combinations.

As for the 6-jet mode, the selection philosophy is basically the same as that explained in Sec. III A 4. Therefore, we only sketch it below. The main difference from the threshold scan is the cut values which must be much tighter to require four-momentum balance, well-reconstructed W's, and t's: $\Delta p_T \leq 12$ GeV, $\Delta p_L \leq 12$ GeV, $E_{\rm vis} \geq 270$ GeV, $|M_{2\ \rm jets} - m_W| \leq 8$ GeV, and $|M_{3\ \rm jets} - m_t| \leq 15$ GeV. The b tagging and the cut on the b-W angle are necessary in addition, as in the lepton-plus-4-jet case.

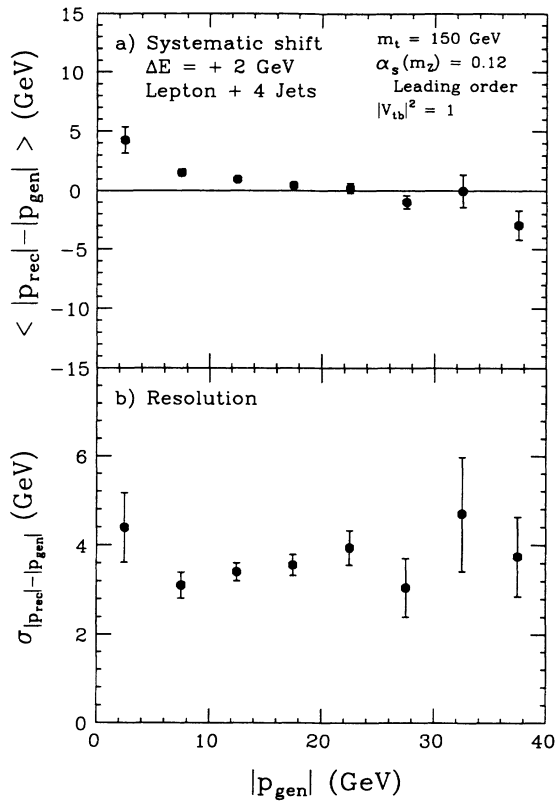

FIG. 23. (a) Systematic shift in the reconstructed top momentum as a function of the generated top momentum. (b) Momentum dependence of the momentum resolution. These figures coresond to Fig. 22.

Monte Carlo simulations resulted in a detection efficiency of 2.2%, including the branching fraction to the 6-jet mode. Since both t and $\bar{t}$ quarks can be used for the momentum measurement, the effective selection efficiency is twice this value. The reconstructed top momentum distribution is shown in Fig. 24(b) (solid circles), which should be compared with the generated one (histogram). The agreement of the reconstructed with the generated is not as good as in the lepton-plus-4-jet case. This is because of the combinatorial background shown as solid squares in the same figure. If we can eliminate the contamination from c jets in the b-jet candidates [25], this combinatorial background can be significantly reduced. At the same time, we can relax the kinematical cuts to gain in the detection efficiency. Although this is an important possibility and worth further studies, we conservatively assume, in what follows, that only the lepton-plus-4-jet mode is usable.

6. *Expected precision*

We have demonstrated above that the top quark momentum is indeed measurable with reasonable resolution

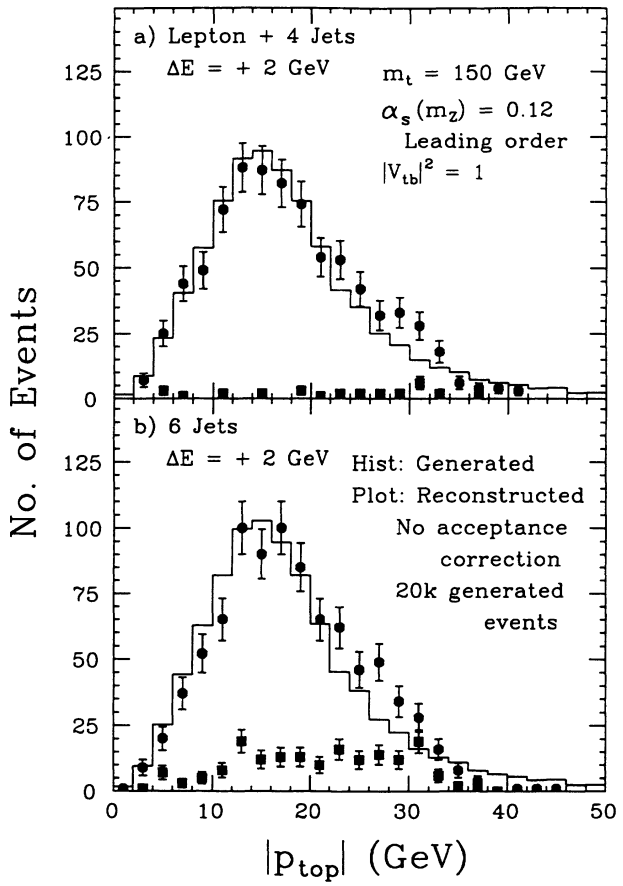

FIG. 24. Reconstructed momentum distribution (solid circles) for (a) the lepton-plus-4-jet mode and (b) the 6-jet mode, compared with the generated distribution (histogram). The solid squares indicate the combinatorial background due to wrong jet assignment. The Monte Carlo events were generated with $\alpha_s(m_Z) = 0.12$ and plotted with no acceptance correction.

and detection efficiency. We can thus estimate the statistical error on the $|\mathbf{p}|_{\mathrm{peak}}$ from the width of the expected momentum distribution and the expected number of reconstructed top quarks. In actual experiments, we need to examine various systematic errors of both theoretical and experimental nature. One of the most serious theoretical ambiguities is due probably to the fact that the top quark has color. In the threshold region, however, the color neutralization is expected to take place between b and $\bar{b}$ quarks. Therefore, the additional uncertainty from possible top-hadron formation is absent. Nevertheless the b-quark fragmentation must be well understood to eliminate the ambiguity introduced when we group particles in the final state into t and $\bar{t}$ sides. We will not try to estimate the systematic errors by extrapolations from the present knowledge. Instead, we discuss only the statistical errors here to demonstrate the potential sensitivity of the momentum measurement to various parameters.

Figure 25(a) plots the momentum distributions at $\Delta E = 2$ GeV for $\alpha_s(m_Z) = 0.11$, 0.12, and 0.13, when $|V_{tb}|^2 = 1$. The dependence of the peak position on $\alpha_s(m_Z)$ at $\Delta E = 2$ GeV is depicted in Fig. 25(b). The dotted lines indicate the 1σ bounds corresponding to an integrated luminosity of 100 fb^{-1}. The expected statistical error on $\alpha_s(m_Z)$ is about 0.0015, in this example, if $\sqrt{s_{1S}}$ is known and $|V_{tb}|^2 = 1$.

Plotted in Fig. 26(a) are the momentum distributions at $\Delta E = 2$ GeV, for $|V_{tb}|^2 = 0.8$, 1.0, and 1.2, when $\alpha_s(m_Z) = 0.12$. The peak position ($|\mathbf{p}|_{\mathrm{peak}}$) increases with $|V_{tb}|^2$ as shown in Fig. 26(b), where again the 1σ bounds are indicated by dotted lines. In this example, $\Delta|V_{tb}|^2 \simeq 0.04$ is expected for 100 fb^{-1}, when $\sqrt{s_{1S}}$ and $\alpha_s(m_Z)$ are known.

C. Measurement of forward-backward asymmetry

So far, we have been concentrating on the S-wave contributions to the Green's function, since the P-wave contributions to the total cross section and the momentum distribution are of $O(\beta^2)$ and, therefore, can be ignored. The P-wave contributions, however, may produce measurable forward-backward asymmetry through the S-P interference as an $O(\beta)$ correction to the differential cross section (see Sec. II).

In this section, we discuss the possible role of the forward-backward asymmetry in parameter determina-

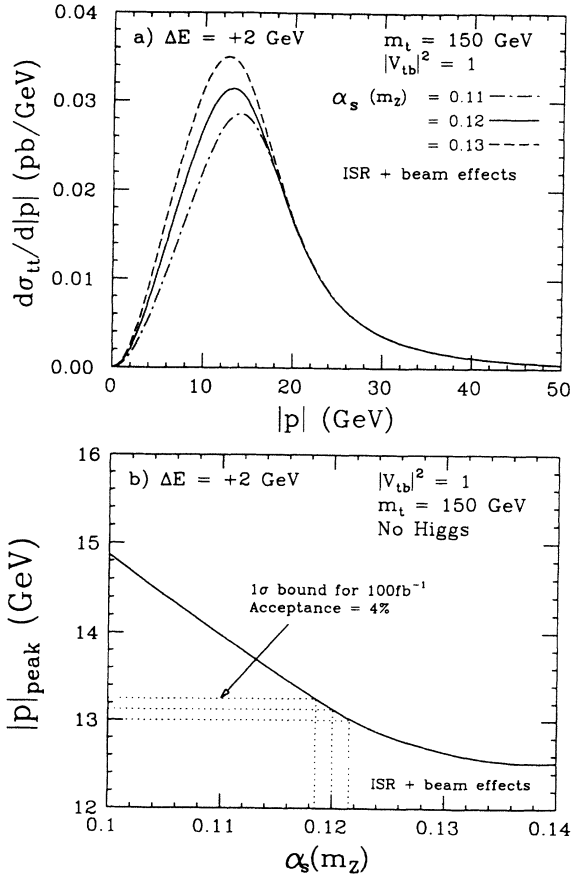

FIG. 25. Top momentum distribution at $\Delta E = 2$ GeV, for $\alpha_s(m_Z) = 0.11$, 0.12, 0.13, and $m_t = 150$ GeV. (b) Momentum peak position as a function of $\alpha_s(m_Z)$. The dotted lines indicate the 1σ bounds expected for an intergrated luminosity of 100 fb^{-1}.

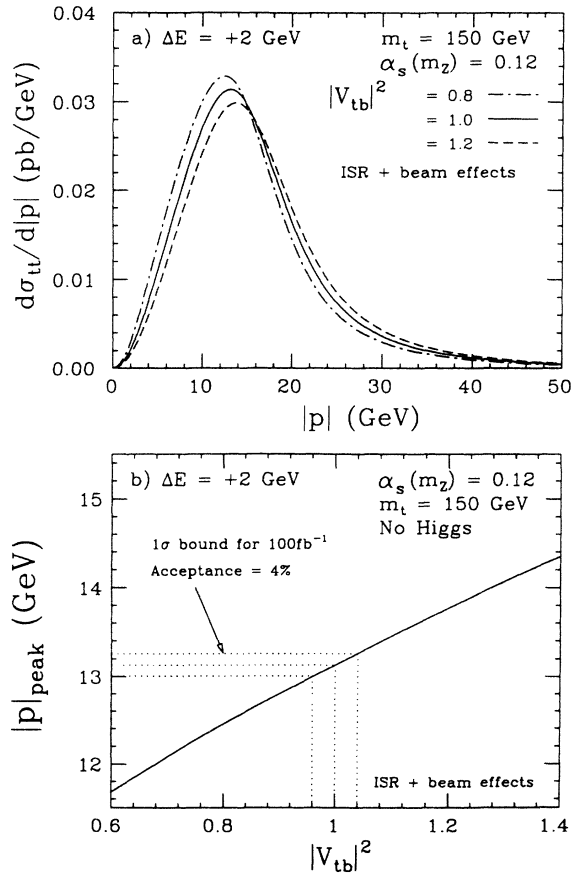

FIG. 26. (a) Similar to Fig. 25 but plotted for different top widths. (b) The momentum peak position as a function of $|V_{tb}|^2$. The dotted lines indicate the 1σ bounds expected for an integrated luminosity of 100 fb^{-1}.

tions. The forward-backward asymmetry of the top quark production is defined explicitly in Appendix A together with the necessary formulas. After examining the relevant parameters that controls the asymmetry, we fix the energy point at which the asymmetry measurement is to be carried out, according to the same criteria as with the momentum measurement described in the preceding section. We then study the sensitivity of the asymmetry measurement to various parameters.

1. Dependence on various parameters

Figure 27 illustrates the locations of the S- and P-wave resonances. The first S-wave resonance ($1S$) stands alone but the second and higher S-wave resonances (nS : $n \geq 2$) are accompanied by P-wave resonances. When the $t\bar{t}$ potential is exactly Coulombic, the S- and P-wave resonances are mass degenerate for $n > 1$. In the case of a realistic QCD potential, the P-wave states, which "feel" the longer distance part of the $t\bar{t}$ potential compared to the S-wave states, acquire larger binding energies and have slightly lower masses. Suppose we sit at the $1S$ peak. Then the S-P interference vanishes if the level splitting between the $1S$ and the $2P$ states is much larger than the widths of the resonances. The level splitting is determined by α_s, while the resonance widths are controlled by the t-quark width. Therefore, we expect that the measurement of the forward-backward asymmetry of the top quark reconstructed from the bW final state allows us to extract additional information on the top width and the strong coupling constant.

Figure 28(a) shows the forward-backward asymmetry as a function of ΔE for $\alpha_s(m_Z) = 0.11$, 0.12, and 0.13, before the inclusion of the beam effects. As expected, the asymmetry at the $1S$ peak gets larger when α_s decreases, though the dependence is rather weak. Figure 28(b), on the other hand, demonstrates the dependence on the top width. The asymmetry is enhanced as the top width grows, since the S-P overlapping becomes more significant. As with the top momentum distribution, the asymmetry is insensitive to m_t, which is demonstrated in Fig. 28(c).

2. Dependence on intermediate-distance potential

Since the intermediate-distance potential has practically no effect on the total cross section, and since the asymmetry is also an integrated quantity, it is expected that the asymmetry is insensitive to the intermediate-distance potential. This is indeed the case as shown in Fig. 29(a) by virtue of the large top width. When the width is artifically reduced to 1/10, the modification of the intermediate-distance potential produces a visible effect on higher resonance states [see Fig. 29(b)].

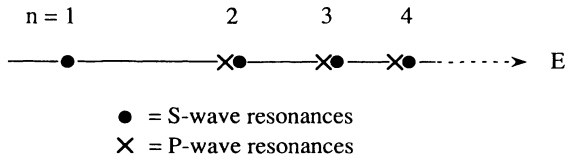

FIG. 27. Schematic showing the locations of the S- and P-wave resonances.

3. Beam effects

Because the main source of the forward-backward asymmetry is the interference among S- and P-wave resonances, the asymmetry depends rather strongly on the energy. This necessitates the proper account of the beam effects. Figure 30 plots the asymmetry as a function of ΔE for the three cases considered for the total cross section and the top momentum measurements. The effect of the ISR is similar to that of beamstrahlung and makes a difference of 10–20 % in the observable asymmetry. The effect of the beam energy spread is significant, about 50%, around the energy corresponding to the minimum asymmetry. There is no particularly preferred energy here in contrast to the momentum measurement case. The asymmetry measurement thus requires the beam effects be properly understood and controlled.

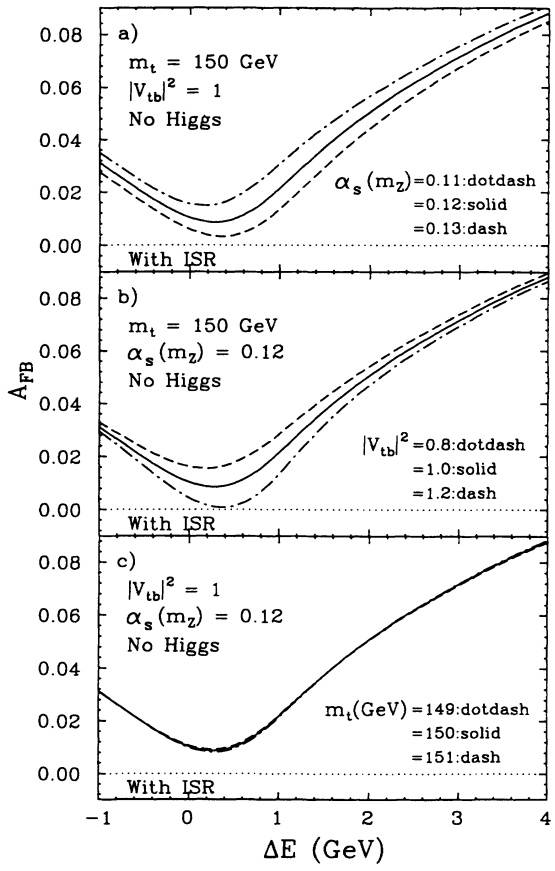

FIG. 28. Forward-backward asymmetry as a function of ΔE, showing the dependence on (a) $\alpha_s(m_Z)$, (b) $|V_{tb}|^2$, and (c) m_t. These include the initial state radiation but not the beam effects.

4. Sensitivity to various parameters

Figures similar to Figs. 28(a)–28(c) are shown in Figs. 31(a)–31(c) after including the beam effects. Figure 31(a) tells us that the best sensitivity to $\alpha_s(m_Z)$ is attained at around $\Delta E = 1$ GeV. As for the width measurement, a slightly lower energy is better as suggested in Fig. 31(b). The dependence on m_t is negligible in practice, given the precision on m_t expected from the threshold scan [see Fig. 31(c)].

We set the energy for the asymmetry measurement at $\Delta E = 1$ GeV below.

5. Expected precision

In order to measure the forward-backward asymmetry, we have to know the charge of the reconstructed 3-jet system. The most straightforward method is the use of the lepton-plus-4-jet final state, for which we can use selection cuts similar to those for the momentum measurements. We must, however, relax the cuts significantly, since the expected asymmetry is rather small and a high statistics sample is necessary. If m_t is larger, the asymmetry becomes larger and the measurement becomes easier.

We might also be able to use the 6-jet final states: we can use the semileptonic decays of heavy flavored mesons for sure. We might even be able to use the D mesons if we can reconstruct secondary vertices. Anyway, all of these require detailed Monte Carlo studies which are heavily detector dependent. We, therefore, restrict ourselves to the discussion of the expected statistical errors on various

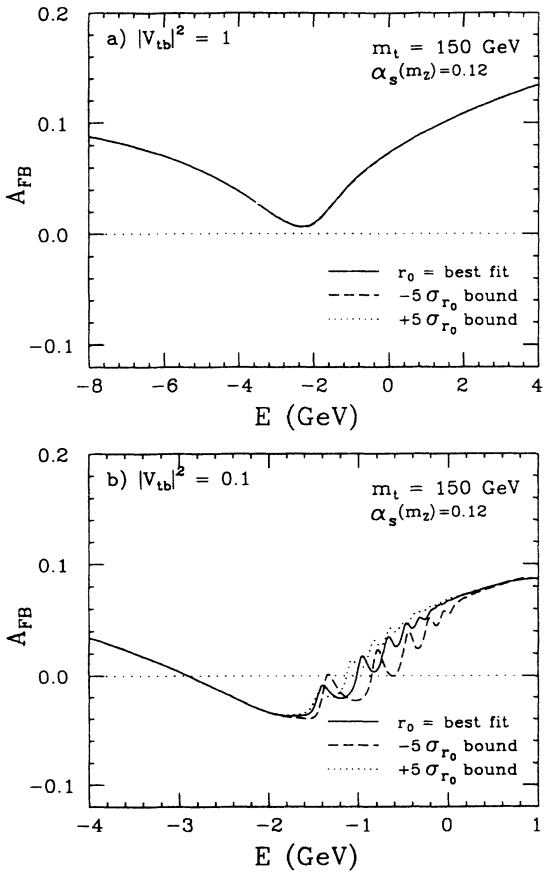

FIG. 29. Dependence of the forward-backward asymmetry on the intermediate-distance potential, before the inclusion of the initial state radiation and beam effects, for (a) $|V_{tb}|^2 = 1$ and (b) $|V_{tb}|^2 = 0.1$.

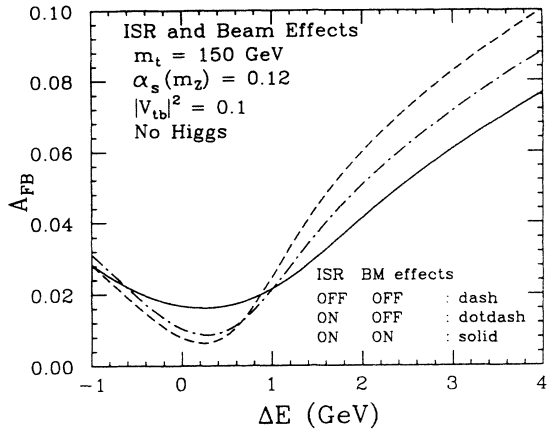

FIG. 30. Effects of the initial state radiation and the beam energy spread and beamstrahlung on the forward-backward asymmetry.

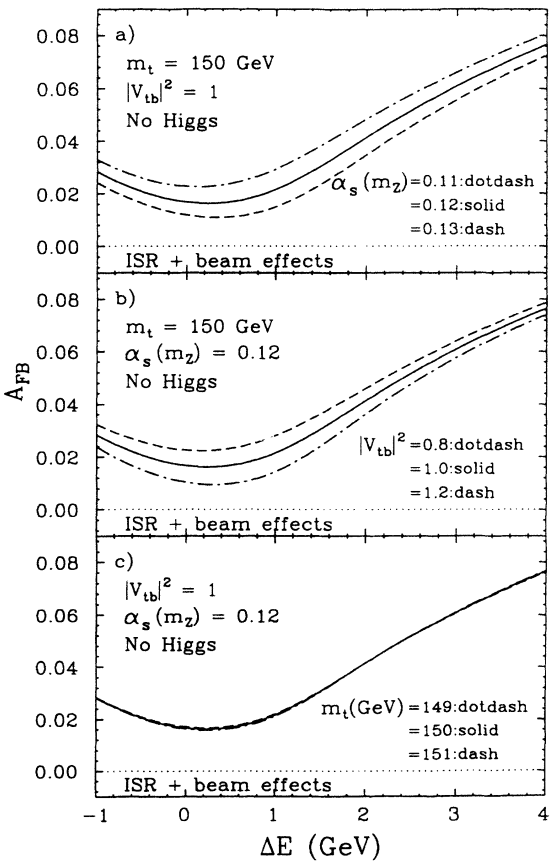

FIG. 31. Similar plots to Figs. 28(a)–28(c) after the inclusion of the beam effects.

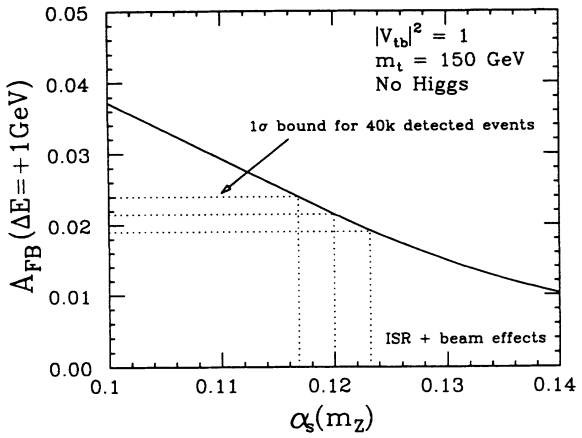

FIG. 32. The forward-backward asymmetry at $\Delta E = 1$ GeV as a function of $\alpha_s(m_Z)$. The dotted lines indicate the 1σ bounds expected for $40k$ reconstructed $t\bar{t}$ events.

parameters, provided that a sample of $40k$ reconstructed events is given. The sample corresponds to 200 fb^{-1}, even if the detection effciency is as high as 40%. Since the asymmetry value is small, the systematic error due to the detector asymmetry must be carefully studied in actual experiments. We expect collider operations at the Z pole will be very useful, since the experimental limit on the measurable asymmetry will be determined by the number of events available for the detector calibration [26].

Figure 32 shows the asymmetry at $\Delta E = 1$ GeV as a function of $\alpha_s(m_Z)$. The dotted lines in the figure indicate the 1σ bounds expected for $40k$ detected events. Unfortunately, the sensitivity to $\alpha_s(m_Z)$ is poor compared to that of the momentum measurement: $\Delta\alpha_s(m_Z) \simeq 0.003$, if $\sqrt{s_{1S}}$ and $|V_{tb}|^2$ are known.

The asymmetry at the same energy is plotted against the normalized top width ($|V_{tb}|^2$) in Fig. 33. If $\sqrt{s_{1S}}$ and $\alpha_s(m_Z)$ are known, $40k$ detected events allow us to determine the top width with a relative statistical error of 7%.

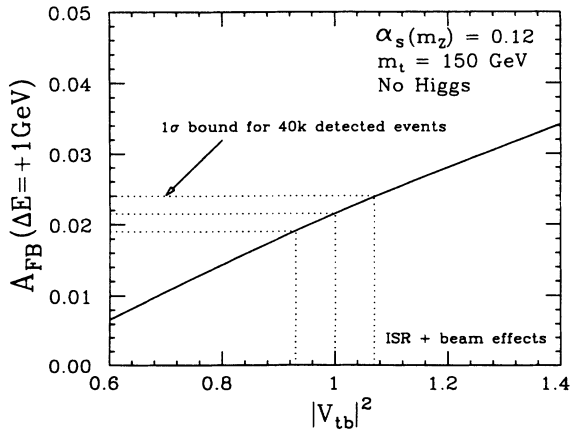

FIG. 33. The forward-backward asymmetry at $\Delta E = 1$ GeV as a function of $|V_{tb}|^2$. The dotted lines indicate the 1σ bounds expected for $40k$ reconstructed $t\bar{t}$ events.

IV. SUMMARY AND CONCLUSION

The large decay width expected for a heavy top quark gives the $t\bar{t}$ threshold essentially new features distinct from that of the lighter $q\bar{q}$ threshold. The large width acts as an infrared cutoff and allows reliable estimates of the QCD contributions to the threshold cross sections, which, in turn, make possible the extraction of other smaller effects such as Higgs-boson-exchange contributions. It should be also noted that event selection can be efficiently carried out by reconstructing the $bW^+\bar{b}W^-$ final states through the jet-invariant-mass method. We have carried out quantitative studies of physics at the $t\bar{t}$ threshold in e^+e^- collisions, using the recently developed theoretical formalism which includes full $O(\alpha_s)$ corrections.

There are many ways to extract physics at the $t\bar{t}$ threshold. We have illustrated the strategy for the experimental studies, taking a sample case of $m_t = 150$ GeV. The results of the studies can be summarized as follows.

We can measure the threshold shape by energy scan. Given 11 energy points with 1 fb^{-1} each, we can determine the top mass with a statistical error of $\Delta m_t = 0.2$ GeV, even if α_s is totally unconstrained. On the other hand, we can expect $\Delta\alpha_s(m_Z) = 0.005$, even if m_t is unknown. The expected statistical error on the top width is $\Delta\Gamma_t/\Gamma_t = 0.2$, when $\alpha_s(m_Z)$ is known. For the standard model Higgs boson of $m_H = 100$ GeV, the expected statistical error on the normalized top Yukawa coupling is $\Delta\beta_H = 0.43$, which can be reduced to $\Delta\beta_H = 0.29$ by doubling the integrated luminosity per energy point or by making use of the lepton-plus-4-jet mode together with the 6-jet mode. These results, however, assume a good control of the beam energy spread, $\Delta E_{\rm beam} \lesssim 0.4\%$ [full width at half maximum (FWHM)], or a precision differential luminosity measurement.

The momentum spectrum measurement at the $t\bar{t}$ threshold is less dependent on the beam effects. It should be emphasized that such a measurement is possible only for the top quark and provides information independent of that from the total cross section measurement. Using the $1S$-peak position determined by the threshold scan, we can perform precision measurements of $\alpha_s(m_Z)$, which are essentially free from the ambiguity caused by the top mass uncertainty. The sensitivity of the top momentum measurement to $\alpha_s(m_Z)$ is expected to be $\Delta\alpha_s(m_z) \simeq 0.0015$ for 100 fb^{-1}, provided that the $1S$-peak position is known. Given the same statistics, we expect $\Delta\Gamma_t/\Gamma_t \simeq 0.04$, provided that the $1S$-peak position and $\alpha_s(m_Z)$ are known from other sources. It should also be noted that the top momentum measurement is insensitive to the Higgs-boson-exchange effects. Therefore the parameters determined from the top momentum measurement can be fed back to the Yukawa coupling extraction from the total cross section.

The forward-backward asymmetry gives additional information on $\alpha_s(m_Z)$ and the top width. $40k$ detected $t\bar{t}$ events provide us with an opportunity to measure $\alpha_s(m_Z)$ with a statistical error of $\Delta\alpha_s(m_Z) \simeq 0.003$,

if the $1S$-peak position and $|V_{tb}|^2$ are known. With the same event sample, we can measure the top width with a statistical error of $\Delta\Gamma_t/\Gamma_t \simeq 0.07$, if the $1S$-peak position and $\alpha_s(m_Z)$ are known. This, however, requires a small beam energy spread or a precise knowledge of the differential luminosity.

ACKNOWLEDGMENTS

The authors wish to thank all the members of the JLC working group for useful discussions and comments. In particular, K. Hagiwara, K. Hikasa, C. Ng, and H. Murayama deserve special mention. The authors are very grateful to Professor P. Igokemenes, Professor M. Jeżabek, Professor J. Kühn, Professor M. Peskin, and Professor P. Zerwas for valuable discussions.

APPENDIX A: CROSS-SECTION FORMULAS

Here, we summarize the formulas necessary for the evaluations of the $t\bar{t}$ production cross sections used in our analysis, which include all the $O(\alpha_s)$ corrections. We present the formulas of the total cross section $\sigma^0_{\rm tot}(e^+e^- \to t\bar{t})$ and the top quark three-momentum distribution $d\sigma^0/d|\mathbf{p}_t|d\cos\theta$ in Sec. A 1. Then the method for including the initial state radiation is explained in Sec. A 2. The effective beam energy spectrum used in our analysis is given in Sec. A 3.

In addition to all the $O(\alpha_s)$ corrections, we include part of the $O(\alpha_s^2)$ corrections to the cross sections given below. These are (1) the two-loop corrections to the QCD potential $V(r)$, and (2) the running of the toponium width $\Gamma_\Theta(E,\mathbf{p})$.

(1) We use the two-loop improved QCD potential $V(r)$ in the Schrödinger equations for the Green's functions, $G(\mathbf{x};E)$ and $F^i(\mathbf{x};E)$, which determine the overall structures of the cross sections in the threshold region. This QCD potential is determined from the two-loop perturbative QCD (improved by renormalization group) in the short-distance part, while the long-distance part is determined phenomenologically. The overall form of the potential is fixed by fitting to charmonium and bottomonium data. Details of the potential can be found in Ref. [9].

(2) We include the phase space suppression effect on the widths of the toponium resonances, which is achieved by using the running toponium width $\Gamma_\Theta(E,\mathbf{p})$ in the Schrödinger equations for the nonrelativistic Green's functions, and also by including the $O(\beta^2)$ terms of the phase space volume of bW's; see the cross-section formulas below. This prescription is important in preserving the unitarity relation between the total cross section obtained from summing the final states and that calculated using the optical theorem. The running toponium width reduces the top quark differential cross section in the highly off-shell region as compared to the constant width approximation, while it enhances the total cross section at the resonance peak [27]. The readers may consult Ref. [9] for the details.

1. Total cross section and top 3-momentum distribution

There are two processes that contribute to the $t\bar{t}$ production cross section up to $O(\alpha_s)$ in the threshold region, namely, $e^+e^- \to bW^+\bar{b}W^-$ and $e^+e^- \to bW^+\bar{b}W^-g$. The following formulas are derived in Ref. [14] and are given as the sum of the cross sections for both of the two processes. The real gluon in the final state, if any, is understood to be associated with $b(\bar{b})$ if the invariant mass of the $bg(\bar{b}g)$ system is smaller than that of the $\bar{b}g(bg)$ system [28]. We neglect the b-quark mass for simplicity.

(a) Total cross section. The total cross section is obtained via the optical theorem

$$\sigma^0_{\rm tot} = \frac{96\pi^2\alpha^2}{s^2}\left\{1 - \frac{4C_F\alpha_s(m_t)}{\pi}\right\}[(Q_eQ_t + v_ev_t\chi)^2 + a_e^2v_t^2\chi^2]{\rm Im}G(\mathbf{x}=0;E=\sqrt{s}-2m_t), \tag{A1}$$

where $C_F = 4/3$ is the color factor and χ is the ratio of photon and Z propagators defined by

$$\chi = \frac{s}{s-m_Z^2}. \tag{A2}$$

The coupling factors are

$$\begin{aligned} v_e &= (-\tfrac{1}{2} + 2\sin^2\theta_W)/(2\sin\theta_W\cos\theta_W), \\ v_t &= (\tfrac{1}{2} - \tfrac{4}{3}\sin^2\theta_W)/(2\sin\theta_W\cos\theta_W), \\ a_e &= -1/(4\sin\theta_W\cos\theta_W), \\ a_t &= 1/(4\sin\theta_W\cos\theta_W), \end{aligned}$$

with $Q_e = -1$ and $Q_t = 2/3$. We set $\alpha = 1/128$, $\sin^2\theta_W = 0.23$, $m_Z = 91.17$ GeV, and $m_W = 80$ GeV in our analyses.

(b) Top 3-momentum distribution. The top quark 3-momentum distribution can be written in the form

$$\begin{aligned} \frac{d\sigma^0}{d|\mathbf{p}|d\cos\theta} &= \frac{d\sigma^0_{t\bar{t}}}{d|\mathbf{p}|d\cos\theta} + \frac{d\sigma^0_{t\bar{t}g}}{d|\mathbf{p}|d\cos\theta} \\ &= \frac{24\alpha^2}{s^2}\frac{\Gamma_\theta(E;\mathbf{p})}{2}|\mathbf{p}|^2(T_0 + T_1\cos\theta), \end{aligned} \tag{A3}$$

where $E = \sqrt{s} - 2m_t$ is the c.m. energy measured from the threshold, $\mathbf{p}$ denotes the 3-momentum of top quark, and θ represents the polar angle of the top momentum measured from the electron beam direction.

The spherically symmetric part (T_0) and the $\cos\theta$ part (T_1) are given, respectively, by

$$T_0 = [(Q_eQ_t + v_ev_t\chi)^2 + a_e^2v_t^2\chi^2]\left[\left\{1 - \frac{4C_F\alpha_s(m_t)}{\pi}\right\}|\tilde{G}(\mathbf{p};E)|^2 + C_F4\pi\alpha_s(\mu_B)\int\frac{d^3\mathbf{q}}{(2\pi)^3}\frac{1}{|\mathbf{q}-\mathbf{p}|^3}2\mathrm{Im}[\tilde{G}^*(\mathbf{q};E)\tilde{G}(\mathbf{p};E)]\frac{\pi}{2}\right], \tag{A4}$$

$$T_1 = (Q_eQ_ta_ea_t\chi + 2a_ev_ea_tv_t\chi^2)\frac{|\mathbf{p}|}{m_t}2\mathrm{Re}[\tilde{F}^*(\mathbf{p};E)\tilde{G}(\mathbf{p};E)] + 2a_ev_t\chi(Q_eQ_t + v_ev_t\chi)\kappa C_F4\pi\alpha_s(\mu_B) \times\int\frac{d^3\mathbf{q}}{(2\pi)^3}\frac{1}{|\mathbf{q}-\mathbf{p}|^3}\frac{\mathbf{p}\cdot(\mathbf{q}-\mathbf{p})}{|\mathbf{p}||\mathbf{q}-\mathbf{p}|}2\mathrm{Re}[\tilde{G}^*(\mathbf{q};E)\tilde{G}(\mathbf{p};E)], \tag{A5}$$

with $\kappa = (1-2r)/(1+2r)$ and $r = m_W^2/m_t^2$. It is understood that the principal value is taken in the loop integral in the second term of Eq. (A5) as $\mathbf{q}\to\mathbf{p}$. The strong coupling constant for the final state interactions is evaluated at the Bohr scale $\mu_B(\sim\alpha_s m_t)$, and we choose $\mu_B = \alpha_s(m_Z)m_t$.

The phase space volume $|\mathbf{p}|^2\Gamma_\Theta(E,\mathbf{p})$ is explicitly factored out together with an appropriate coefficient, where the running toponium width $\Gamma_\Theta(E,\mathbf{p})$ is given in terms of the top quark width Γ_t:

$$\frac{\Gamma_\Theta(E,\mathbf{p})}{2} = \Gamma_t\left[1 + \tilde{\eta}_1\left(\frac{E}{m_t}\right) - \tilde{\eta}_2\left(\frac{\mathbf{p}^2}{m_t^2}\right)\right] \tag{A6}$$

with

$$\tilde{\eta}_1 = 3\frac{1+r+2r^2}{1+r-2r^2},\quad \tilde{\eta}_2 = \frac{1}{6}\frac{13+13r+46r^2}{1+r-2r^2}, \tag{A7}$$

and

$$r = \frac{m_W^2}{m_t^2}. \tag{A8}$$

Here, the top quark width including $O(\alpha_s)$ corrections is given by [29]

$$\Gamma_t = \frac{G_F}{\sqrt{2}}\frac{m_t^3}{8\pi}(1+2r)(1-r)^2\left\{1 - \frac{C_F\alpha_s(m_t)}{2\pi}h(r)\right\} \tag{A9}$$

with

$$h(r) = \pi^2 + 2\mathrm{Li}_2(r) - 2\mathrm{Li}_2(1-r) + [2(5+4r)(1-r)^2\ln(1-r) + 4(1+r)(1-2r)r\ln r - (1-r)(5+9r-6r^2)]/[2(1-r)^2(1+2r)]. \tag{A10}$$

The S-wave and the P-wave Green's functions, $\tilde{G}(\mathbf{p};E)$ and $\tilde{F}(\mathbf{p};E)$, are determined by solving the inhomogeneous Schrödinger equations in the coordinate space, and then taking their Fourier transforms [30]:

$$\left[-\frac{\nabla^2}{m_t} + V(r) - \left(E + i\frac{\Gamma_\Theta}{2}\right)\right]G(\mathbf{x};E) = \delta^3(\mathbf{x}), \tag{A11}$$

$$\tilde{G}(\mathbf{p};E) = \int d^3\mathbf{x}\, e^{-i\mathbf{p}\cdot\mathbf{x}}G(\mathbf{x};E), \tag{A12}$$

and

$$\left[-\frac{\nabla^2}{m_t} + V(r) - \left(E + i\frac{\Gamma_\Theta}{2}\right)\right]F^k(\mathbf{x};E) = -i\partial^k\delta^3(\mathbf{x}), \tag{A13}$$

$$p^k\tilde{F}(\mathbf{p};E) = \int d^3\mathbf{x}\, e^{-i\mathbf{p}\cdot\mathbf{x}}F^k(\mathbf{x};E). \tag{A14}$$

Technical details of the method to solve these for the Green's functions can be found in Refs. [4,9,11].

Noting that the S-wave Green's function $\tilde{G}(\mathbf{q};E)$ is only dependent on $|\mathbf{q}|$, the angular part of the loop integrations $\int d^3\mathbf{q}/(2\pi)^3$ can be performed analytically in Eqs. (A4) and (A5), and they may be reduced to one-parameter integrals using the formulas

$$\int\frac{d^3\mathbf{q}}{(2\pi)^3}\frac{1}{|\mathbf{q}-\mathbf{p}|^3}f(q) = \frac{1}{4\pi^2p}\int_0^\infty dq\, w_0(q/p)f(q), \tag{A15}$$

$$\int\frac{d^3\mathbf{q}}{(2\pi)^3}\frac{1}{|\mathbf{q}-\mathbf{p}|^3}\frac{\mathbf{p}\cdot(\mathbf{q}-\mathbf{p})}{|\mathbf{p}||\mathbf{q}-\mathbf{p}|}f(q) = \frac{1}{4\pi^2p}\int_0^\infty dq\, w_1(q/p)f(q), \tag{A16}$$

with

$$w_0(x) = x\left[\frac{1}{|x-1|} - \frac{1}{x+1}\right], \tag{A17}$$

$$w_1(x) = \frac{1}{2}\left[P\frac{1}{x-1} + \frac{2x+1}{x+1} - x\ln\left|\frac{x+1}{x-1}\right|\right], \tag{A18}$$

for any function $f(q)$ and $q = |\mathbf{q}|$, $p = |\mathbf{p}|$.

(c) Forward-backward asymmetry. The forward-backward asymmetry is defined by

$$A_{\rm FB} = \frac{N_{\rm F} - N_{\rm B}}{N_{\rm F} + N_{\rm B}}, \tag{A19}$$

where $N_{\rm F}$ and $N_{\rm B}$ are the numbers of top quarks produced with $\cos\theta > 0$ and $\cos\theta < 0$, respectively. In the absence of the initial state radiation and the beam effects, the theoretical prediction for the asymmetry can be obtained from Eq. (A3) as

$$\begin{aligned} A^0_{\rm FB} &= \frac{1}{\sigma^0_{\rm tot}}\int_0^\Lambda d|\mathbf{p}|\left[\int_0^1 d\cos\theta - \int_{-1}^0 d\cos\theta\right]\frac{d\sigma^0}{d|\mathbf{p}|d\cos\theta} \\ &= \int_0^\Lambda d|\mathbf{p}||\mathbf{p}|^2 T_1\Gamma_\Theta(E;\mathbf{p}) \Big/ 2\int_0^\Lambda d|\mathbf{p}||\mathbf{p}|^2 T_0\Gamma_\Theta(E;\mathbf{p}), \end{aligned} \tag{A20}$$

where the momentum cutoff Λ is defined by

$$\Lambda^2 = \frac{1}{16m_t^2}(9m_t^2 - m_W^2)(m_t^2 - m_W^2). \tag{A21}$$

2. Inclusion of initial state radiation

It is well known that the initial state radiation has to be properly taken into account in the vicinity of a resonance state. We include this by convoluting the differential cross section without the initial state radiation ($d\sigma^0$) with the radiator function introduced in Ref. [31]:

$$d\sigma = \left[1 + \frac{2\alpha_0}{\pi}\left(\frac{\pi^2}{6} - \frac{1}{4}\right)\right]\int_0^1 dz\,\beta_e\left[z^{\beta_e - 1}\left(1 + \frac{3}{4}\beta_e\right) - \left(1 - \frac{z}{2}\right)\right]d\sigma^0(\hat{s}), \tag{A22}$$

where

$$\begin{aligned} \hat{s} &= s(1-z) \\ \beta_e &= \frac{2\alpha_0}{\pi}\left[\ln\left(\frac{s}{m_e^2}\right) - 1\right]. \end{aligned} \tag{A23}$$

The fine structure constant α_0 is taken to be 1/137 here, since the relevant energy scale is of low energy.

3. Beam energy spread and beamstrahlung

In order to study experimental feasibilities in a realistic environment, we need to include the effects due to beam energy spread and beamstrahlung. In this paper we assume that the primary e^+e^- beams have a uniform energy spread of 1.0% in FWHM, unless otherwise stated. On the other hand, the fractional beam energy (ϵ) after beamstrahlung is given by the following formulas, when normalized to the energy before the beamstrahlung [32]:

$$\Psi(\epsilon) = \int_0^1 d\tau e^{-N_\gamma\tau}\left(\delta(\epsilon - 1) + \frac{e^{-y}}{1-\epsilon}H(N_1\tau y^{1/3})\right) \tag{A24}$$

with

$$\begin{aligned} N_\gamma &= N_{\rm cl}U_0(\xi_1), \\ N_{\rm cl} &= 1.06\alpha_0 r_e N\frac{2}{\sigma_x + \sigma_y}, \\ U_0(\xi) &= \frac{1 - 0.598\xi + 1.061\xi^{5/3}}{1 + 0.922\xi^2}, \\ \xi_1 &= \frac{r_e^2 E_0 N}{\alpha_0 m_e \sigma_z}\frac{2}{\sigma_x + \sigma_y}, \\ H(x) &= \left(\frac{3}{8\pi}\right)^{1/2}\left[\frac{\sqrt{x/3}}{1 + 0.53x^{-5/6}}\right]^{3/4}\exp[4(x/3)^{3/4}], \\ y &= \frac{1}{\xi_1}\left(\frac{1}{\epsilon} - 1\right), \\ N_1 &= \frac{1}{1+\xi_1 y}N_{\rm cl} + \frac{\xi_1 y}{1+\xi_1 y}N_\gamma, \end{aligned} \tag{A25}$$

where r_e and m_e are the electron classical radius and the electron mass, respectively, E_0 is the nominal beam energy, N is the number of particles per bunch, and σ_x, σ_y, and σ_z are the bunch size at the interaction point.

The energy spectra of the e^+e^- beams after beam-

strahlung are obtained by convoluting the primary flat energy distribution with the one given by the above formulas. The relevant beam-related parameter values used in this paper are $E_0 = 150$ GeV, $N = 0.63 \times 10^{10}$, $\sigma_x = 0.335$ μm, $\sigma_y = 0.00392$ μm, and $\sigma_z = 85$ μm, which were cited from Ref. [24]. Figure 5 shows the resultant effective center-of-mass energy distribution. The sharp peak at $\sqrt{s_{\rm eff}}/\sqrt{s_0} = 1$ [the δ-function part in Eq. (A24)] corresponds to the no beamstrahlung case, while the long tail downwards is due to beamstrahlung photons.

APPENDIX B: MONTE CARLO EVENT GENERATION

When the top width exceeds a typical hadronization scale, there will be no t-hadron formation [33]. Then the polarization information of parent top quarks is transferred to decay daughters, which gives rise to angular correlations in the final state particles. In order to take proper account of this effect, we should use the full helicity amplitudes. As for the color neutralization, we assume that the color flux is spanned between b and $\bar{b}$ quarks. Since we are going to reconstruct top quarks by jet-invariant-mass method, it is also important to consider gluon emissions from b or $\bar{b}$ quarks as well as those from W decay daughters. The point here is the energy scale to be used for the parton showering from b or $\bar{b}$ quarks. We should not, for instance, set $Q_{\rm max} = \sqrt{(p_b + p_{\bar{b}})^2}$, but, instead, should set $Q_{\rm max} = m_t - m_W$, since the gluon emission is controlled by the acceleration the b or $\bar{b}$ quarks receive when their parent t or $\bar{t}$ quarks decay. Consequently, the 4-momentum adjustments after parton showering should be made within the bW systems. Namely, the b and the $\bar{b}$ quarks radiate gluons independently [34]. The gluon emissions from t or $\bar{t}$ quarks, which are not included here, could modify the event shape: only the leading-order threshold correction is implemented in our Monte Carlo event generator [35] and, therefore, the generated top momentum distribution in Figs. 24(a) and 24(b) are slightly different from the calculation with full $O(\alpha_s)$ corrections. Nevertheless, the gluon emissions from the t and $\bar{t}$ quarks affects the detection efficiency only at the level of $O(\alpha_s)$ and can be ignored when we estimate statistical errors on various parameters. It is also essential to include initial state radiations as well as beam energy spread and beamstrahlung, since they may change the event shape significantly. In order to take all of these effects into account, we have used the HELAS system [36] for helicity amplitude calculations and the BASES-SPRING system [37] for phase-space integrations and event generations. The generated Monte Carlo events were processed through a detector simulator which simulates the response of the model detector described in Ref. [24].

[1] CDF Collaboration, Phys. Rev. Lett. **68**, 447 (1992).

[2] ALEPH, DELPHI, L3, and OPAL:LEP Collaborations, Phys. Lett. B **276**, 247 (1992).

[3] V. Fadin and V. Khoze, Yad. Fiz. **48**, 487 (1988) [Sov. J. Nucl. Phys. **48**, 309 (1988)].

[4] M. Strassler and M. Peskin, Phys. Rev. D **43**, 1500 (1991).

[5] S. Komamiya, in *Research Directions for the Decade*, Proceedings of the Summer Study on High Energy Physics, Snowmass, Colorado, 1990, edited by E. Berger (World Scientific, Singapore, 1991), p. 459.

[6] K. Fujii, in *Proceedings of the Second Workshop on JLC, Tsukuba, Japan, 1990*, edited by S. Kawabata (KEK Report No. 91-10, Tsukuba, 1991), p. 271.

[7] K. Fujii, in *Physics and Experiments with Liner Colliders*, Proceedings of the Workshop, Saariselkä, Finland, 1991, edited by R. Orava, P. Eerola, and M. Nordberg (World Scientific, Singapore, 1992), p. 203.

[8] R. Miquel, in *Physics and Experiments with Linear Colliders* [7]; see also in e^+e^- *Collisions at 500 GeV: The Physics Potential*, Proceedings of the Workshop, Hamburg, Germany, 1991, edited by P. Zerwas (DESY Report No. 92-123A, Hamburg, 1992), p. 327.

[9] Y. Sumino, K. Fujii, K. Hagiwara, H. Murayama, and C. Ng, Phys. Rev. D **47**, 56 (1993).

[10] M. Jeżabek, J. Kühn, and T. Teubner, Z. Phys. C **56**, 653 (1992).

[11] H. Murayama and Y. Sumino, Phys. Rev. D **47**, 82 (1993).

[12] K. Melnikov and O. Yakovlev, Phys. Lett. B **324**, 217 (1994); V. Fadin, V. Khoze, and A. Martin, Phys. Rev. D **49**, 2247 (1994); Phys. Lett. B **320**, 141 (1994).

[13] Y. Sumino, in *Proceedings of the Workshop on Physics and Experiments with Linear e^+e^- Colliders*, Waikoloa, Hawaii, 1993, edited by F. A. Harris, S. L. Olsen, S. Pakvasa, and X. Tata (World Scientific, Singapore, 1993), p. 439.

[14] K. Hikasa, S. Ishihara, and Y. Sumino (in preparation); Y. Sumino, Ph.D. thesis, University of Tokyo, 1993.

[15] Although our Monte Carlo event generator does not include all of the next-to-leading order corrections (see Appendix B), we used it only to estimate detector resolution and acceptance effects. Consequently, only the raw (without acceptance correction) Monte Carlo data after selection cuts (Figs. 8 through 12 and Figs. 22 through 24) do not take into account all of the next-to-leading order corrections, while all the other figures are results from the full next-to-leading order calculations.

[16] In the threshold region, typical velocity of an unstable top quark is $\beta \sim (\Gamma_t/m_t)^{1/2} \sim \alpha_s$.

[17] It is a virtue of the threshold region that there is no ambiguity in deciding where to span the color flux; it should be spanned between b and $\bar{b}$, since gluons with wavelength $\sim \Lambda_{\rm QCD}^{-1}$ would not be able to resolve the color charges of t and $\bar{t}$.

[18] V. Fadin and V. Khoze, Proceedings of the 24th LNPI Winter School, Leningrad, 1989 (unpublished).

[19] M. Jeżabek and J. Kühn, Phys. Lett. B **316**, 360 (1993).

[20] C. Quigg and J. Rosner, Phys. Rep. **56**, 167 (1979).

[21] The best fit value of r_0, the connection point of the short- and the intermediate-distance potentials, is $r_0 = 0.235 \pm 0.010$ GeV^{-1} for $\alpha_s(m_Z) = 0.12$, where the indicated error corresponds to one standard deviation. See Ref. [9] for details.

[22] M. Frary and D. Miller, in e^+e^- *Collisions at 500 GeV: The Physics Potential* [8], p. 379.

[23] M. Jeàzbek, J. Kühn, and T. Teubner, in *Proceedings of the Workshop on Physics and Experiments with Linear* e^+e^- *Colliders* [13].

[24] JLC Group, KEK Report 92-16, 1992 (unpublished).

[25] The contamination from c jets can be eliminated by explicitly requiring both secondary and tertiary vertices, instead of just demanding a large impact parameter. In order to assure reasonable detection efficiency, this necessitates a high resolution vertex detector.

[26] T. Omori, in *Proceedings of the Workshop on Physics and Experiments with Linear* e^+e^- *Colliders* [13].

[27] It is argued [10] that the Coulomb enhancement effect on the resonance widths may cancel the phase space suppression effect so that the use of constant width may be more appropriate. While this argument should be examined carefully, we incorporate the phase space suppression effect in this paper, since the consistent treatment of total and differential cross sections in the Monte Carlo simulation is indispensable and cannot be achieved with the constant width approximation.

[28] This corresonds to setting $y = y_{\max}$ in the formulas given in Ref. [14].

[29] M. Jeżabek and J. Kühn, Nucl. Phys. **B314**, 1 (1989); A. Czarnecki, Phys. Lett. B **252**, 467 (1990); J. Liu and Y.-P. Yao, Int. J. Mod. Phys. A **6**, 4925 (1991); C. Li, R. Oakes, and T. Yuan, Phys. Rev. D **43**, 3759 (1991).

[30] The method to obtain $\tilde{G}(\mathbf{p}; E)$ directly by solving the Schrödinger equation in momentum space has also been developed [10].

[31] See, for instance, F. Berends, in *Z Physics at LEP I*, Proceedings of the Workshop, Geneva, Switzerland, 1989, edited by G. Altarelli, R. Kleiss, and C. Verzegnassi (CERN Yellow Report No. 89-08, Geneva, 1989), Vol. 1.

[32] K. Yokoya, Proceedings of 1988 Linear Accelerator Conference (CEBAF Report No. 89-001, 1989), p. 494.

[33] J. Kühn, Acta Phys. Austriaca, Suppl. **24**, 203 (1982); I. Bigi, Y. Dokshitzer, V. Khoze, J. Kühn, and P. Zerwas, Phys. Lett. **181B**, 157 (1986); T. Sjöstrand and P. Zerwas, in e^+e^- *Collisions at 500 GeV: The Physics Potential* [8], p. 463.

[34] Y. Dokshitzer, V. Khoze, L. Orr, and W. Stirling, Nucl. Phys. **B403**, 84 (1993).

[35] We implemented in our Monte Carlo event generator the threshold enhancement by attaching to the $t\bar{t}V$ ($V = \gamma$ or Z) vertex the S-wave Green's function of the Schrödinger equation [see Eqs. (A11) and (A12)] together with the hard-gluon correction factor $1 - 4C_F\alpha_s/\pi$. Those corrections which are not included in the event generator are the $O(\alpha_s)$ correction to the top width, the final state interactions, the P-wave contribution to the $t\bar{t}Z$ vertex, and the real gluon emission off the t and $\bar{t}$ quarks.

[36] H. Murayama, I. Watanabe, and K. Hagiwara, KEK Report No. 91-11, 1992 (unpublished).

[37] S. Kawabata, Comput. Phys. Commun. **41**, 127 (1986).